Università di Genova

Scuola di Scienze Matematiche, Fisiche e Naturali

PhD thesis

Design and synthesis of new Layered Double Hydroxides (LDHs) as new electrodes materials in lithium-ion batteries and post lithium devices

CHEMICAL SCIENCES AND TECHNOLOGIES

XXXVI Cycle

Tutor:

Dr. Anna Maria Cardinale

Candidate:

Marco Fortunato

"The case only helps readymade minds"

Louis Pasteur

Table of Contents

Acknowledgments

I would like to thank my supervisor Dr. Anna Maria Cardinale for the continuous support both for the human and academic point of view. Specially, I appreciate her tendency to let me free to choose in which way orienteering my project and believe my ideas. I thank her, and the PhD program, for letting me go to schools, conferences and for the abroad period.

I would thank my abroad supervisor Dr. Sonia Dsoke, Dr Angelina Sarapulova, Dr. Xinyue Li, Dr. Bjorn Schwarz and all the other PhD students for their great support and their teaching activity during my period at the Karlsruhe Institute of Technology.

I thank also all the members of the inorganic chemistry group, specially all the PhD and master students that helped to make this period so enjoyable.

Finally, I thank my family without whom I would have never had this opportunity.

Abstract

The electrification is the most probable strategy to overcome the raising problems due to the consumption of fossil fuels, but several energy storage systems are needed to complete the task. Among them rechargeable batteries play a key role for the automotive sector and their relevance is rising also for stationary applications as grid storage; in both cases the current technologies present sustainability issues related to the supply of raw materials.

In this work was investigated the applicability of a new family of compounds, Layered double hydroxides (LDHs), as active anodic material both in lithium (LIBs) and sodium (SIBs) rechargeable ion batteries.

Several materials were preliminary tested in LIBs following a "trial and error" approach and, among them only NiAl-NO_3 and NiFe-NO_3 LDHs gave enough satisfactory results to be deeper investigated.

For what concern LIBs, a combined study involving classical electrochemical analysis and thermo-analytical techniques was used to explain the influence of the LDH structure on the electrochemical performances of NiFe-NO_3. It was demonstrated that the presence of a bidimensional feature helps the stabilization of the material leading to high performances with a lower amount of the electrochemically active Ni.

Both NiAl-NO_3 and NiFe-NO_3 were tested in SIBs, demonstrating their applicability in these devices.

The second one was discovered to be much more stable upon the charge/discharge loops retaining a high specific capacity (~ 500 mAh/g) after 50 cycles. This discrepancy was explained, through a deep and detailed study, including *in operando* techniques, enlightening the stabilizing role of iron and the presence of reversible reactions involving the nitrate. The reaction mechanism for NiFe-NO_3 was proposed, it was made of an initial irreversible "activation" reaction in the first sodiation followed by a mixed intercalation/conversion reversible mechanism in the following cycles.

In the end, some other applications for LDHs were presented: FeMg-Cl was discovered as a potential catalyst to produce formic acid, while NiAl-citrate was investigated both for the absorption of the toxic Pb^{2+} from waters both as catalyst precursor. Through a pyrolysis, in fact, NiAl-citrate evolves into a metallic-Ni based material with a very high specific area (177 m^2/g) that was tested as catalyst for the dry reforming of methane.

Abstract (Italian Version)

Per superare i crescenti problemi legati al consumo di combustibili fossili la strategia attualmente più popolare è l'elettrificazione, ma per completare il processo sono necessari diversi sistemi di stoccaggio energetico. Tra questi le batterie ricaricabili già oggi rivestono un ruolo capitale per il settore automobilistico e stanno diventando fondamentali anche per le applicazioni stazionarie come il *grid storage*. in entrambi i casi però le attuali tecnologie presentano problemi di approvvigionamento delle materie prime.

In questo lavoro è stata studiata l'applicabilità di una nuova famiglia di composti, i *layer double hydroxides* (LDHs), come materiali attivi per anodi sia nelle batterie ricaricabili agli ioni di litio (LIBs) che di sodio (SIBs).

È stato seguito un approccio *"trial and error"* per testare diversi materiali in LIBs, tra questi solo NiAl-NO_3 e NiFe-NO_3 LDH hanno dato risultati abbastanza soddisfacenti per essere studiati in maniera più approfondita

Per quanto riguarda i sistemi al litio è stato condotto uno studio combinato che coinvolge classiche analisi elettrochimiche e tecniche termo-analitiche per spiegare l'influenza della struttura degli LDH sulle prestazioni anodiche del NiFe-NO_3. È stato dimostrato che la bidimensionalità aiuta la stabilizzazione dell'elettrodo e porta ad alte prestazioni con una minore quantità di materiale attivo (nichel).

Sia NiAl-NO_3 che NiFe-NO_3 sono stati testati, dimostrandosi applicabili, in SIBs.
Il NiFe-LDH si è dimostrato molto più stabile nei cicli di carica e scarica rispetto NiAl-NO_3 mantenendo un'elevata capacità specifica (~ 500 mAh/g) anche dopo 50 cicli.
Attraverso uno studio approfondito e dettagliato, comprendente anche tecniche in-operando, è stata spiegata questa discrepanza mettendo in luce il ruolo stabilizzante del ferro e la presenza di reazioni reversibili che coinvolgono il nitrato. Inoltre, è stato proposto un meccanismo di reazione per NiFe-NO_3. Questo è costituito da una reazione iniziale irreversibile "di attivazione" durante la prima sodiazione, mentre nei cicli successivi è presente un meccanismo reversibile misto di intercalazione/conversione.

In fine sono presentate alcune altre applicazioni degli LDHs: FeMg-Cl si è comportato come potenziale catalizzatore per la produzione di acido formico, mentre NiAl-citrato è stato studiato, sia per l'assorbimento dalle acque del Pb^{2+} sia come precursore di un catalizzatore. Attraverso la pirolisi, infatti, NiAl-citrato evolve in un materiale a base di Ni metallico con un'area specifica molto elevata (177 m^2/g) che è stato testato come catalizzatore per il *dry reforming* del metano.

Table of abbreviations

In the following manuscript there will be present several abbreviation and acronyms, all explicated in the text at the first appearance, to make the reading more comfortable is presented here below a table with all of them in alphabetical order.

BET	Brunauer–Emmett–Teller
CE	Coulombic Efficiency
CV	Cyclic Voltammetry
DC	Direct Current
DRM	Dry Reforming of Methane
EV	Electric Vehicle
EXAFS	Extended X-ray Absorption Fine Structure
FBR	Fixed Bed Reactor
FC	Field Cooled
FE-SEM	Field Emission-Scanning Electron Microscope
FT	Fourier Transform
FT-IR	Fourier Transform-InfraRed
GC-MS	Gas Chromatography-Mass Spectrometry
GCPL	Galvanostatic Cycling with Potential Limitation
HCOOH	Formic acid
HOMO	Highest Occupied Molecular Orbital
ICE	Inner Combustion Engine
ICL	Irreversible Capacity Loss
ICP-OES	Inductively Coupled Plasma-Optical Emission Spectroscopy
LDH	Layered Double Hydroxide
LIB	Lithium-Ion Battery
LUMO	Lowest Occupied Molecular Orbital
NaAlg	Sodium alginate
pp	Polypropilen
PPMS	Physical Property Measurement System
PVDF	PolyVinylidene DiFluoride
PXRD	Powder X-Ray Diffraction
RC	Rate Capability
SEI	Solid Electrolyte Interface
SIB	Sodium-Ion Battery
TCD	Thermal Conductivity Detector

TEM	Transmission Electron Microscopy
TGA	ThermoGravimetric Analysis
TG-DTA	ThermoGravimetry-Differential Thermal Analysis
VSM	Vibrating Sample Magnetometry
XANES	X-ray Absorption Near Edge Structure
XAS	X-ray Absorption Spectroscopy
XRF	X-Ray Fluorescence
ZFC	Zero Field Cooling

1. Introduction

The rapid increasing of population in the last century and the general life-style improvement, especially in emerging countries, has led to a large consumption of fossil fuels connected to several environmental problems such as the increasing of greenhouse gasses and the subsequent increase of the mean temperature (fig. 1)*(1)*.

Nowadays the two main challenges to reduce the human impact on the planet are the substitution of fossil fuels by sustainable energy sources, for the electricity production, and the replacing of internal combustion engines (ICEs) with electric vehicles (EVs) for transportation.

The sources of sustainable energy are naturally discontinued and requires energy storage systems to homogenize the power distribution, namely, batteries. Although, in recent years the sustainable harvesting systems have made great strides, especially in the fields of photovoltaics and wind, the development of suitable storage mechanisms is still immature. Furthermore, the most promising technology for the vehicle electrification is again batteries, hence, the development of cells with long term stability, very prolonged cycle life and made of conflict-free materials is one of the key problems in electrochemistry*(2,3)*.

The most interesting kind of batteries nowadays are the rechargeable metal ion batteries, in particular lithium-ion batteries (LIBs) seem the perfect solution for both the previous issues even if they are still to be improved and a lot of work has to be done on all their main constituents. Unfortunately, the lithium demand is bound to rapidly exceed supply, so it is important to found also other technologies able to bear the burden of the challenge*(4,5)*. The obvious answer to this question is the most similar element to lithium, namely sodium, that could be exploited in the same way in sodium ion batteries (SIBs). The main problem is that sodium is bigger and heavier than lithium and so are its devices

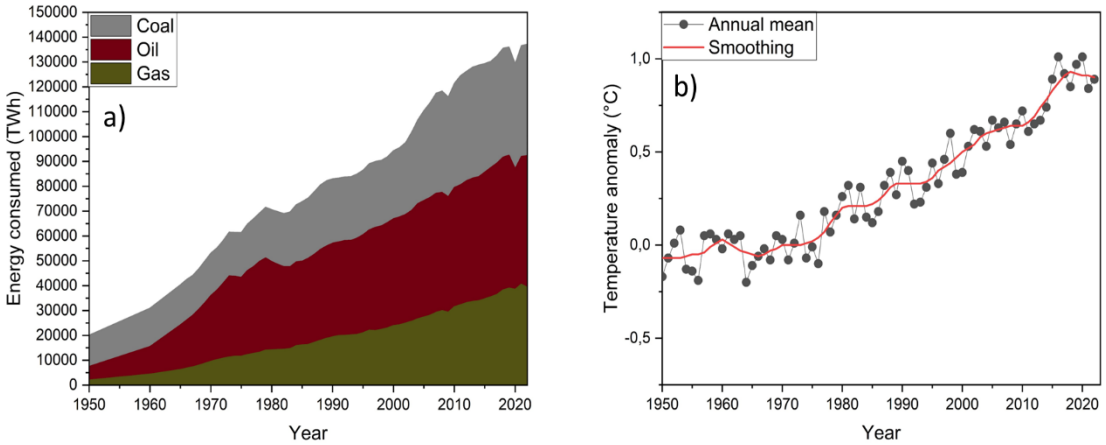

Figure 1: global trends. a) World power consumption by fossil fuels. b) Earth surface temperature anomaly in comparison to the long-term average (1951-1980). Both graphs are referred to the period 1950-2023

in comparison with LIBs making them not suitable for EVs, nevertheless they could play a key role for what concern stationary applications such as grid storage*(6)*.

1.1. Metal ion Batteries: characteristic, components, and functioning

A metal ion battery consists in the following main components: a positive (cathode) and a negative (anode) electrode connected by a circuit and separated from an electrolyte able to host the ions. Usually, the two electrodes are separated by a physical membrane (separator) to prevent the short-circuit of the battery. During the discharging process, metal ions move from the anode to the cathode through the electrolyte. Simultaneously the associated electrons flow from the anode to the cathode through the external circuit. Conversely, during the recharging process, the metal ions and electrons are forced to move in the opposite way by an external load, all the process is schematized in figure 2. In this process the reduction and oxidation are inverted but by convention, in rechargeable batteries, the positive electrode could be called anode and the negative one cathode independently if the battery is under charge or discharge.

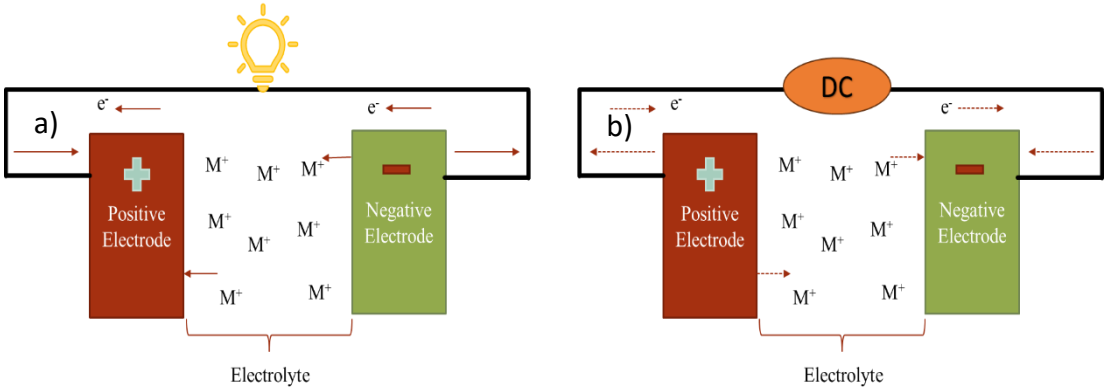

Figure 2: scheme of a metal ion battery in discharge a) and charge b)

The focus of this study is the synthesis and applications of anodic materials tested in a half cell configuration (will be better explained in next chapters) so in this introduction there will be only an overview on currently studied anodic materials and the main reactions that involve the electrolyte.

1.1.1. Anodic materials

The main features to consider when thinking about an anode, for any kind of metal ion batteries, are low redox potential, stable structure (to maintain integrity and improve cycle stability), high electrical and ionic conductivity (to have a fast charge and discharge), great availability, ease of preparation, cost-effectiveness, and environmental friendliness.

The anodic materials can be classified into three main groups according to the way with they react with metal ions (M^+) during the charge/discharge process, as shown in figure 3.

- *Insertion reaction mechanism*: the ions move to the compound and are hosted in the interstices; the mechanism is described in equation 1.

$$AB_x + yM^+ + ye^- \rightleftarrows M_yAB_x \qquad (eq.1)$$

Among this group of materials, the carbon-based anodes are predominant, existing in many forms with different morphologies and chemical composition. This kind of anodes always show stability at different temperatures and in several chemical and electrochemical environments, they also have a low cost of productions*(7)*. The first material discovered and studied for the intercalation of Li^+ was graphite, it shows a reversible capacity of more than 350 $mAhg^{-1}$ and a high coulombic efficiency (CE)[a] and nowadays it is the standard for commercial batteries*(8)*. To increase its electrochemical properties, several modifications of the morphology and particle size are being tried, graphene, carbon nanotubes and nanofibers were widely studied*(7,9)*.

Are worthy of a special mention the so-called hard carbon materials that are proving to be very performing (specific capacity between 400 and 1000 $mAhg^{-1}$) and are slowly substituting graphite. Furthermore, in recent years they start to be produced by biomass from the perspective of the circular economy*(10)*.

Another interesting set of anode material is the titanium-based oxides, completely constituted by TiO_2 polymorphs which show low price, low toxicity, very low volume expansion during cycling, very good cycling life, a stable operating voltage at 1,55 V but a very low specific capacity (175 mAg^{-1})*(11)*.

For what concern SIBs, graphite could not be used since sodium couldn't be hosted*(12)*, so hard-carbon materials are the "first generation" of electrodes tested and applied on SIBs; reaching a specific capacity of ≈300 mAhg-1. They display a little ICL, but after 50 cycles the 70 % of capacity is retained also at high current*(13)*. Also in this case, titanium-based materials such as TiO_2, $Li_4Ti_5O_{12}$, $Na_2Ti_3O_7$, and $NaTi_2(PO_4)_3$ were deeply studied, in fact, they can reversibly store sodium in an intercalation/de-intercalation cycle with a sufficient cyclic stability, proper working plateaus and quite good energy density*(14)*.

- *conversion reaction mechanism*: transition metal oxides or sulphides (Z) are used as anodes; they react with M^+ to form MnZ and the pure metal as described in equation 2.

$$A_x^{(n)}Z_y + yM^+ + ye^- \rightleftarrows xA + yM_nZ \qquad (eq.2)$$

The theoretical capacity of the conversion-reaction-based anode materials for LIBs is very wide and move from the low range of 350 $mAhg^{-1}$ for Cu_2S to the high range of 1800 $mAhg^{-1}$ for MnP_4*(15)*. Even this class of compounds displays some major drawbacks that shall be considered: First, their columbic efficiency is lower than the one

[a] Coulombic efficiency (CE) describes the charge efficiency by which electrons are transferred in batteries. CE is the ratio of the total charge extracted from the battery to the total charge put into the battery over a full cycle.

of carbon compounds and tends to decrease with cycling. Moreover, the volume expansion induces the pulverization of the material limiting its working life. At last, the operating voltage reaches a plateau at a higher value than the graphite; that phenomenon leads to a lower energy density than the one expected. To mitigate these problems two strategies are usually chosen: the preparation of nano-scaled porous materials (to avoid the volume expansion) and the combination with carbonaceous materials (to improve the capacity and give a buffer space able to host the expansion)*(16)*.

The same situation happens in SIBs, the materials show very high capacity but undergoes several volume changes limiting their applicability, currently are under investigation to try to mitigate this problem*(17)*.

- *alloying reaction mechanism*: a direct reaction between M^+ and A forming a new compound like in equation 3.

$$A + yM^+ + ye^- \rightleftarrows M_yA \qquad (eq.3)$$

Lithium metal holds one of the highest capacities among anodic materials (3860 $mAhg^{-1}$), but the safety issue is a great problem, because of the dendrite formation, which limits the use of lithium as anode material in rechargeable batteries. One way to avoid this problem is to use materials which can satisfy the requirement of high capacity, for example, silicon, silicon monoxide and tin oxide which react with lithium with an alloying/de-alloying mechanism*(18)*. Their theoretical capacity achieves outstanding value (in some case more than 3000 $mAhg^{-1}$), but their development is blocked by their low cycling life and the considerable volume expansion during the reaction*(19)*.

In SIBs silicon is not suitable due to an extreme volume expansion but is demonstrated that the alloying process can occur with tin and some binders which have the function to buffer the volume expansion. Such Tin-electrodes show a specific capacity of 200

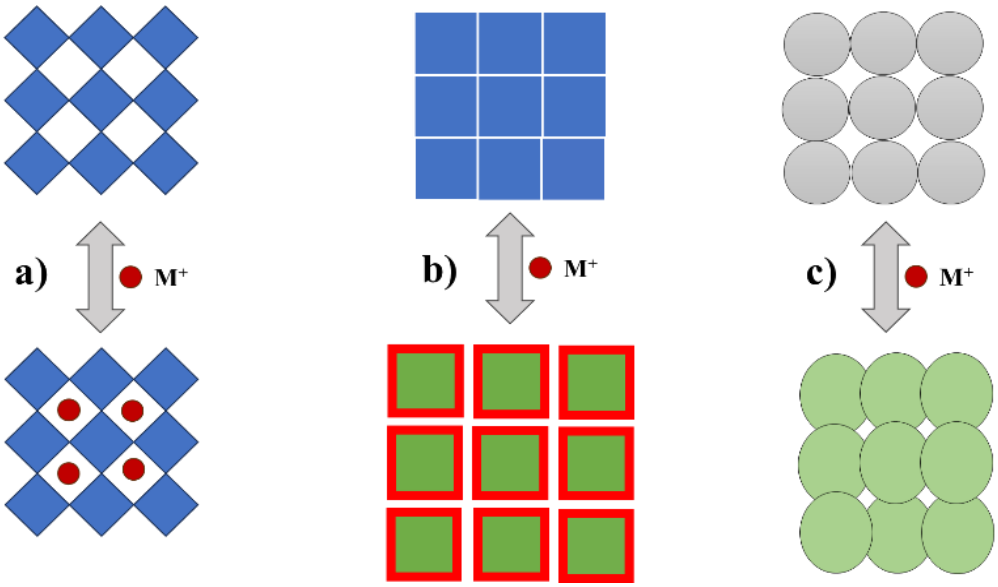

Figure 3: different kinds of reaction mechanisms a) insertion; b) conversion; c) alloying.

$mAhg^{-1}$ also after 20 cycles*(20)*, also antimony*(21)* and red phosphorous*(22)* are under investigation.

1.1.2. Electrolyte

Currently almost all the commercial electrolytes are non-aqueous solutions of a metallic salt, organic carbonates, and several additives. In recent years the focus is moving, due to safety issues, to aqueous or solid-state electrolytes, but until now those technologies are still immature to be applied on a large scale.

As concerns non aqueous electrolytes, one of the most relevant reactions that happen during the first cycles is solid electrolyte interface (SEI) formation.

At the surface of the anode, occur the following two main processes: the reaction with M^+ (Li^+, Na^+…) and the decomposition of part of the electrolyte, leading to the formation of an interface between the liquid electrolyte and the bulk material of the electrode (SEI). The SEI formation is an irreversible process linked with a loss of cell capacity, known as ICL (irreversible capacity loss). Ideally, SEI is a passivating compact layer, able to prevent the penetration of solvated M ions and electrolyte in the defects of the surface leading to an exfoliation (responsible of a marked ICL) and, at the same time, SEI layer must be sufficiently ionically conductive to allow the circulation of M^+ ions*(23)*.

The formation of SEI layer occurs when the redox potential of the electrodes lies outside the electrochemical window of the electrolyte as reported by Goodenough *(24)*. When the lowest unoccupied molecular orbital (LUMO) of the electrolyte is more energetic than the Fermi energy of the anode, the electrolyte is stable; if not, the electrolyte can be reduced.

Similarly, the electrolyte can be stable if the highest occupied molecular orbital (HOMO) of the electrolyte is lower than the cathode Fermi energy level*(25)*.The process is summarised in figure 4.

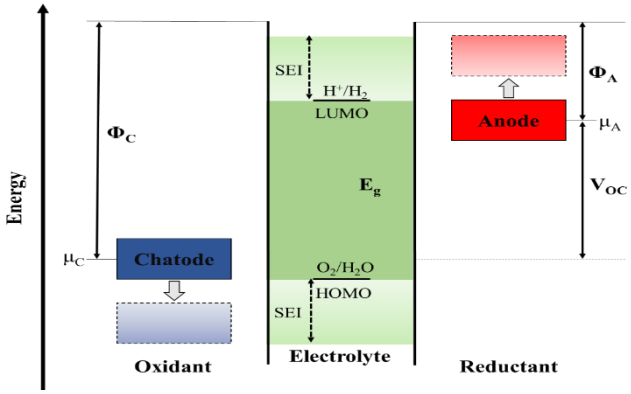

Figure 4: schematic open circuit (OC) energy diagram of an electrolyte. Φ_A and Φ_C are the anode and cathode work function, E_g is the electrolyte's stability window, μ_A and μ_C are the redox potential of anode and cathode.

As seen in this brief introduction for both LIBs and SIBs much work must be done to obtain a good anode able to conjugate high specific capacity, cycling stability, human, environmental and economical sustainability. To face with these issues, is important not

only to improve the current materials, but also to investigate new families of compounds. this study focuses on the analysis of the large group of the layered double hydroxides.

1.2. Layered double hydroxides (LDHs)

1.2.1. Characteristic and applications

Layered double hydroxides (LDHs) are an interesting class of 2D lamellar compounds, their general formula is reported in equation 4*(26)*.

$$[M_{1-x}^{2+}N_x^{3+}\cdot(OH)_2]^{x+}\left(A_{\frac{x}{n}}^{n-}\right)^{x-}\cdot mH_2O \qquad (eq.4)$$

M: divalent metallic cation

N: trivalent metallic cation

A: anion with n- charge

X: molar ratio $\frac{N}{N+M}$

M: a number from 1 to 4.

In literature it's reported the existence of LDHs made of M^{+} or M^{4+} cations but are limited only to Li and Ti*(27,28)*.

The structure of an LDH can be described as brucite[a] layers where a fraction of the Mg^{2+} ions is replaced with a trivalent cation, leading to a positive charge on the surface, which needs a balancing anion at the interlayer. These $M^{2+}/M^{3+}(OH)_6$ octahedra form 2D sheets via edge-sharing and may be connected sheet to sheet by hydrogen bonding between the OH groups. The molar ratio X usually is a value ranging between 0.2 and 0.33, greater values imply that some $M(III)$ octahedron are directly connected reducing the crystallinity.

LDHs could crystallize in two different polymorphs belonging to the space groups $R\bar{3}m$ and $P63/mmc$. However, the presence of stacking faults often leads to mixed phases

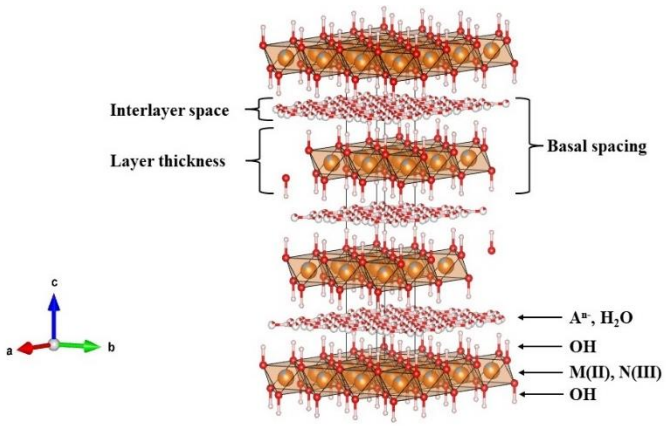

Figure 5: schematic structure of an LDH

[a] Mineralogical name of natural magnesium hydroxides

and/or turbostratic[a] ones*(29)*. A schematic representation of the LDH structure is shown in figure 5.

The first discovered LDH was hydrotalcite[b] , it was found in 1842 by Hochstetter in some schist*(30)*; only 100 years after, in 1942, Feitknecht et al. *(31)* managed to synthetise an analogue MgAl-LDH of the natural compound, but the structure model was confirmed only in 1969 by Almann et al.*(32)*. In the 1990s, thanks to new analytical techniques and advanced characterization tools the properties of LDHs where widely investigated and categorised by the work of Cavani et al.*(26)* that open a wide range of applications for those materials. The bidimensional morphology, the possibility to tune the composition and nature of N, M and A, the ability to intercalate a wide range of different compounds make this class of materials remarkably interesting in different research fields, also very different from each other.

Several studies focus on the remediation of wastewater through LDHs from contaminants and pollutants, such as chromates*(33)*, phosphates*(34)*, dyes*(35)*, surfactants*(36)* and even some radionuclides*(37)*. Another important industrial application is as building materials additives: calcium based LDHs are used in construction concrete to increase both the compressive and flexural strengths and to protect the reinforcement from corrosion, in fact LDH could fill the porosity and simultaneously capture the chloride anions and release protecting agents*(38)*. MgAl-CO_3 LDH is widely studied as flame retardant, it is indeed usually very hydrated and in firing condition it degrades producing a barrier of CO_2 and water vapor, leaving metal oxides as residues that reduce the oxygen supply to the material under the burning surface*(39)*. Since the early 2000s the easy surface modification, biodegradability, pH-sensitivity response, excellent biocompatibility, and anion exchange capacity attract different researchers to the bio applications of LDHs*(40)*. The first reported medical use is as stomach pH regulators*(41)* but as the years go by, they were exploited in a wide range of biomedical studies from drug/gene delivery and tumor imaging to biosensing, anti-bacteria, and tissue engineering*(40,42,43)*.

LDHs were also widely studied as catalyst or catalyst precursor: hydrotalcite is a perfect alkaline template for the catalytic aldolic condensation*(26)*, Ni based LDHs are studied in steam reforming*(26)* and in the water splitting reaction*(44)* ,while Cu based ones usually are used as precursors*(45,46)*.

In the last two decades the increasing interest for new energy storage systems to overcome the challenge of ecological transition has prompted the interest of scientists to new and more efficient materials, among them LDHs could play a key role. In 2006 Wang et al.*(47)* for the first time tested a CoAl-LDH as positive electrode in a supercapacitor, showing specific capacitance of 77 Fg^{-1} and a 90 % energy retention after 1000 cycles of

[a] A crystal structure in which basal planes have slipped out of alignment

[b] Mineralogical name of $Mg_6Al_2(OH)_{16}CO_3{\cdot}4H_2O$.

charge/discharge. Since then, several different compositions where tested and nowadays some LDH-composite materials could reach specific capacity > 2000 Fg^{-1}*(48)*.
In very recent time the layered structure also suggests some potential applications in rechargeable ion batteries, but very few works were done in this direction until now. For what concern LIBs some Ni based compounds were tested as negative electrodes displaying a very high initial capacity > 2000 $mAhg^{-1}$, followed by a high irreversible capacity loss and then a stabilization at > 500 $mAhg^{-1}$ after 100 cycles of discharge/charge *(48–50)*.
Some preliminary studies are nowadays focusing on the applications of LDHs also in SIBs, starting from the pioneering work of Zhao et al. that in 2019 reported for the first time CoFe-NO_3 LDH as a new intercalation type anode for sodium*(51)*.
Finally, is worthy of mention, the study of Yin et al. for the application of NiFe-Cl LDH as a stable and very efficient cathode in Chloride ion batteries*(52)*.

1.2.2. LDHs synthesis

LDHs could be synthesized in different ways, obtaining different morphologies and particle dimensions. In this work were synthetized several compounds, with specific techniques due to the nature of the ions involved. In the next points will be highlighted the main characteristic of each technique that will be presented in this work.

- Coprecipitation: it is the most common and used synthetic route, it is easy, quick, and scalable for industrial purposes. In the coprecipitation technique, aqueous solutions of M^{2+} (or blends of M^{2+} species) and N^{3+} (or mixtures), containing the anion intended for inclusion into the LDH, are employed as precursors. Among the multiplicity of LDH systems involving M(II)/N(III), certain exhibit an adjustable composition concerning the M(II)/N(III) ratio, whereas specific phases can only be achieved within a limited range of ratios; another intriguing aspect of this preparatory technique is that almost all anions can be directly inserted between the hydroxylated layers.
  To ensure the simultaneous coprecipitation of two or more cations, it is essential to carry out the synthesis under supersaturation conditions, typically to achieve supersaturation a strict control of the solution pH is required. Specifically, precipitation should occur at a pH that is equal to or higher than the pH at which the most soluble hydroxide in the solution undergoes precipitation. After this step a thermal treatment is frequently carried out to enhance yields and/or the crystallinity of amorphous or poorly crystallized materials. The conventional aging procedure involves heating the reactor, containing an aqueous suspension of the LDH product, at a temperature ranging from 50 to 100 °C for some hours or days*(53,54)*. The coprecipitation mechanism depends on the condensation of the metal exa-aquo complexes in the solution, to build the brucite-like layers. These sheets exhibit a consistent arrangement of both metallic cations and solvated interlamellar anions. Two frequently employed approaches for coprecipitation are precipitation at low

supersaturation and precipitation at high supersaturation*(26)*. The low supersaturation procedure involves gradually introducing a mixed solution of divalent and trivalent metal salts into a reactor containing an aqueous solution of the desired interlayer anion. Simultaneously, a second solution of an alkali is added into the reactor at a controlled rate to maintain the pH at a predetermined value (usually between 8 and 10), facilitating the coprecipitation of the two metallic salts. The interlayered anion should exhibit a strong affinity for the LDH layers and be in surplus, to avoid competing reactions that may lead to the incorporation of counter-anions from the metal salts. For this reason, metal nitrates and chloride salts are frequently employed due to the low selectivity of LDHs towards these anions. Additionally, LDHs show a pronounced affinity for carbonate anions, so unless carbonate is the intended anion, reactions are typically conducted under nitrogen to prevent the absorption of atmospheric carbon dioxide, which could generate carbonate ions in situ. In the high supersaturation technique, a mixed solution of M(II) and N(III) metallic salts is directly added to an alkaline solution containing the chosen interlayered anion in a one pot process. It usually led to the formation of less crystalline materials due to the high number of crystallization nuclei, furthermore, because this method involves a violent change in the pH of the solution, the formation of impurity, such $M(OH)_2$ and/or $N(OH)_3$ phases, often results. For this reason, is always compulsory a thermal treatment after the synthesis to homogenize the material.

- Urea hydrolysis and hydrothermal method: urea is well known to be a precipitating agent as it is a very weak Brönsted base, it is highly soluble in water and a temperature-controlled hydrolysis in aqueous solutions can produce ammonium cyanate and, if the hydrolysis is prolonged, CO_2 (eq. 5-7).

$$H_2N - CO - NH_2 \xrightarrow{\Delta T} NH_4^+ + NCO^- \quad (eq.5)$$

$$NCO^- + 2H_2O \rightarrow NH_4^+ + CO_3^{2-} \quad (eq.6)$$

$$NCO^- + 2H_3O^+ \rightarrow NH_4^+ + H_2CO_3 \quad (eq.7)$$

The decomposition of urea leads to a pH~9, that is a precondition to the LDHs precipitation, the main advantage of using urea instead of other bases is that the urea hydrolysis progresses slowly causing a low degree of super saturation during precipitation*(55)*

These reactions generate several gas species and if the synthesis is conducted in an autoclave lead, tuning the temperature, is possible to obtain different pressures (from 1 to more than 10 atm) which in turn affect the crystallinity and microstructure of the material. This technique is only suitable for metals that form insoluble inorganic hydroxides such as Al or Mg*(56)*.

- Rehydration exploiting structural memory effect: the calcination of LDH, done at the proper temperature (typical for each LDH), induces the elimination of interlayer

water, hydroxyl groups and anions resulting in a mixture of metal oxides not obtainable with other techniques. This mixture could reform the LDH structure if exposed to water and anions. Water is taken up to reconstruct the hydroxyl layers, while anions and H_2O molecules being assimilated into the interlayer galleries*(57,58)*. The integrated anions are not restricted to those present in the initial LDH material, making this a crucial approach to obtain LDH with low affinity or unusual anions at the interlayer, along with pillared structures. Through this procedure is avoided the competitive intercalation of inorganic anions coming from the metal salts*(59)*. The process is more intricate compared to coprecipitation, often leading to the concurrent generation of amorphous phases. It is essential to recognize that both the calcination temperature and the chemical composition of the LDH sheets exert a substantial influence on the reconstruction process*(54)*. The higher the calcination temperature of the parent LDH, the lower the "memory effect", this is due to the solid-state diffusion of divalent cations into tetrahedral positions facilitating the gradual formation of stable spinels*(42,59)*.

- Modified solvothermal method: this technique is very interesting since could lead to the formation of single layered LDHs. In this method a solution of metallic acetates and sodium citrate was treated with the proper amount of base (determined by titration experiments) and maintained under reflux at a temperature of ~ 90 °C for 3 d. The reaction mechanism is based on the formation of polynuclear metallic citrate clusters that act as germinating agent for the LDHs, while the presence of acetate woks as buffer for the pH. The crystal formation is very slow and forms a very homogeneous suspension of single layered hexagonal plates with a length of ~200 nm and a thickness of ~ 2/3 nm*(60)*. These characteristics are very interesting for different application such as catalysis, but the variety of LDHs obtainable is limited only to the metals able to originate the citrate polynuclear clusters, as Ni and Zn*(61,62)*.

2. This study

This work focusses on the synthesis and direct application of layered double hydroxides electrodes in metal ion batteries.

The materials preparation and some preliminary tests on LIBs were done at the *Department of Chemistry and Industrial Chemistry* of the University of Genova (DCCI*)* while the more in-depth analysis and the tests in SIBs were done at the *Institute of Applied Materials - Energy Storage Systems* (IAM-ESS) *at the Karlsruhe Institute of Technology* (KIT) in Karlsruhe (DE) under the supervision of Dr. Sonia Dsoke.

In literature are reported very few studies about LDHs' direct application in electrochemical cells, so was followed a "trial and error" approach, starting from preliminary tests on different LDHs as anodic materials in half-cells and deeply investigating only the promising ones.

The best candidates were two nickel-based materials, NiAl-NO_3 and NiFe-NO_3; the first one was analyzed in LIBs by dr. Xinyue Li in her PhD project, while the results on SIBs are presented here. The analysis and tests on the second compound both in LIBs and SIBs are the core of this dissertation. Furthermore, NiFe-NO_3 was deeply studied by an intern for the absorption of CrO_4^{2-}, the spent material (from now NiFe-CrO_4), was also applied in SIBs in the perspective of the circular economy thinking about the probable electrochemical activity of Cr.

In the final part of this manuscript are presented some applications of other LDHs, in different side projects as ions exchanger, catalyst, and catalyst precursors.

2.1. Materials and methods

2.1.1. Chemicals

All the chemical used are summarized in table 1.

Table 1: list of all the chemicals used and their purity.

Name	Formula	Purity (mass%)
Aluminium nitrate nonahydrate	$Al(NO_3)_3 \cdot 9H_2O$	ACS reagent, ≥ 98 %
Iron nitrate nonahydrate	$Fe(NO_3)_3 \cdot 9H_2O$	ACS reagent, ≥ 98 %
Nickel nitrate hexahydrate	$Ni(NO_3)_2 \cdot 6H_2O$	Puriss. p.a., ≥ 98.5%
Nickel acetate tetrahydrate	$Ni(CH_3O_2)_2 \cdot 4H_2O$	Purum p.a., ≥ 99 %
Iron chloride	$FeCl_3$	Puriss. p.a., ≥ 98.5 %, (anhydrous)
Magnesium chloride	$MgCl_2$	Puriss. p.a., ≥ 98.5 %, (anhydrous)
Ethanol	CH_3CH_2OH	Absolute, ≥ 99.8 %
Trisodium citrate dihydrate	$Na_3HC_6H_4O_7 \cdot 2\ H_2O$	ACS reagent, ≥ 98 %
Urea	$OC(NH_2)_2$	Puriss, p.a., ≥ 98.5 %
Isopropanol	$CH_3CHOHCH_3$	Purum p.a., ≥ 97 %
Sodium hydroxide	NaOH	Reagent grade, ≥ 98 % (anhydrous)
Conductive carbon C65	……	Commercial battery grade by TIMCAL, ≥ 99.5 %
Ethylene carbonate (EC)	$(CH_2O)_2CO$	Purum p.a., ≥ 99.8 %
Dimethyl carbonate (DMC)	$(CH_3O)_2CO$	Purum p.a., ≥ 99.8 %
Lithium hexafluorophosphate	$LiPF_6$	Commercial LP30, 1M battery grade solution in EC/DMC, ≥ 99.5 %
Sodium perchlorate	$NaClO_4$	ACS reagent, ≥ 98 % (anhydrous)
Fluoroethylene carbonate (FEC)	$CH_2OCHFOCO$	battery grade, ≥ 99.5 %
Sodium alginate	$(NaC_6H_7O_6)_n$	Purum p.a., ≥ 99.8 %

The used water was deionized with an ion exchange unit (M3/M6 Chemical Bürger s.a.s, Genova, Italy), boiled and gurgled with argon to completely avoid the presence of carbonates and CO_2 in the system if necessary.

2.1.2. Experimental

In this chapter will be briefly described the synthetic route and following processes used to obtain the LDHs and their derived compounds.

- NiAl-NO_3: The material was synthesized through the hydrothermal route, a solution has been prepared by dissolving 30 mmol of nickel nitrate hexahydrate ($Ni(NO_3)_2 \cdot 6H_2O$), 45 mmol of urea ($CO(NH_2)_2$), and 15 mmol of aluminum nitrate nonahydrate $Al(NO_3)_3 \cdot 9H_2O$ (Ni:Al ratio of 2:1) in 150 mL of deionized water. This solution was then put in a 200 mL autoclave at 100 °C for 24 h. Finally, the compound was filtered, washed by centrifugation, dried and grinded.
- NiFe-NO_3: The $\left[Ni^{2+}_{0,66}Fe^{3+}_{0,33}(OH)_2\right]^{0,33+}(NO_3^-)^{0,33-}$ was synthetised following the high supersaturation pathway proposed by Gregoire et al. *(63)*, a mixed solution of Ni and Fe in the due proportion was titrated with a 0,5 M solution of NaOH, in a protect atmosphere. The obtained solid precursor was let to rest with its mother liquor in a closed bottle under argon for 3 d at 70 °C. after that the compound was filtered washed several times with deionised water and dried.

  Four aliquots of the compound were annealed with a furnace (Carbolite elf 11/6B) for 4 h respectively at 250 °C, 360 °C and 560 °C.
- MgFe-Cl: the material from now (MFC-1) was prepared with a high supersaturation approach as described by Wu et al.*(64)*

  In a balloon, under continuous Ar flux (3 L/min), 250 mmol of $MgCl_2$ and 125 mmol of $FeCl_3 \cdot 6H_2O$ were dissolved in 250 mL of deionized water, and the pH was adjusted to 12.6 with a solution of NaOH dropwise leading to the formation of a colloidal mixture of metal hydroxides. The so-obtained precipitate with his parent solution was stored under Ar atmosphere, in a dark bottle, (to avoid photocatalyzed side reactions) in an oven at 85 °C for 2 h leading to the recrystallization of the solid and the formation of the LDH structure. The obtained compound was washed with deionized water and separated by centrifugation (2 min, 7500 rpm) several times till the pH of the upper liquid reached the value of 7. The LDH was dried in oven overnight at 60 °C and then grinded to a grain size lower than 125 μm.

  An aliquot of MFC-1 underwent a 4 h treatment at 400 °C to eliminate interlayer compounds, resulting in a calcinated compound (MFC-calc), which is a mixture of metal oxides not yet crystallized. MFC-calc was then subjected to treatment with a 1 M Cl^- aqueous solution, prepared using boiled water, under an argon atmosphere in a mixing machine. This process aimed to reform the layered double hydroxide (LDH) structure with the Cl^- anion incorporated at the interlayer. Following the mixing step, the solid was filtered, washed with deionized water,

and dried at 60 °C overnight. Subsequently, it was ground similarly to MFC-1. From now the obtained material will be labeled as MFC-mem.

- NiAl-citrate: It was produced with the "hydrolytic polymerization" method dissolving 0.4 mmol of $Al(NO_3)_3 \cdot 9H_2O$ and 1.2 mmol of $Ni(CH_3CO_2)_2 \cdot 4H_2O$ in 160 mL of deionized water within a 250 mL flask. To the metals solution were added 1.6 mmol of $Na_3C_6H_5O_7 \cdot 2H_2O$ (470.6 mg), pre-solubilized in 4 mL of water. The whole reaction system was heated to 80 °C for one hour, cooled down to room temperature and titrated with 30 mL of 0.1 M NaOH solution dropwise with vigorous stirring. The solution was transferred into a 250 mL round flask, then heated under reflux under argon atmosphere at 90 °C for 72 h. The resulting LDH was collected by centrifugation at 7000 rpm for 10 min, washed twice with distilled water, and dried under vacuum overnight at 40 °C.

  Two aliquots of 0.1 g of the so obtained compound were used for absorption tests; they were left in batch equilibration overnight in 50 mL of Pb^{2+} contaminated solution, centrifuged at 7000 rpm for 10 min and then the supernatant was collected.

  Another part of the pristine material underwent annealing at 530 °C, immediately after the last endothermic peak, in a tubular furnace (Carbolite GHA 12/300) for a duration of 2 h. To eliminate oxygen, the chamber was purged with argon flux for 30 min before initiating the heating process, and this condition was sustained throughout the entire experiment.

2.1.3. Instruments

The materials were characterized by means of different techniques:

- Powder X-ray diffraction (PXRD): the patterns were recorded using a powder diffractometer (X'Pert MPD, Philips, Almelo, Netherland) equipped with a Cu anticathode ($K_{\alpha 1}Cu = 1.5406$ Å). The indexing of the diffraction data was performed in comparison with the literature using the software package WinPLOTR*(65)*.

- Field Emission Scanning Electron Microscopy (FE-SEM): the samples were observed with a ZEISS SUPRA 40 V microscope, applying an acceleration voltage of 5 kV for 50 s.

- Fourier Transformed Infra-Red (FT-IR) spectroscopy: the spectra ranging from 4000 to 600 cm^{-1} were obtained utilizing a Spectrum 65 FT-IR Spectrometer (PerkinElmer, Waltham, MA, USA). The instrument was equipped with a KBr beam-splitter and a DTGS detector, and an ATR accessory with a diamond crystal was employed for data collection.

- Inductively coupled plasma-Optical emission spectroscopy (ICP-OES): The experiments were conducted utilizing a Varian Vista PRO (Springvale, Australia) with an axially oriented configuration. The sample introduction setup included a pneumatic nebulizer of the glass concentric K-style type (Varian) connected to a glass cyclonic spray chamber (Varian).

- X-ray fluorescence (XRF): the analyses were done using a M4 TORNADO micro-XRF by Bruker.

- Transmission electron microscopy (TEM): A JEM 1011 - 100 kV microscope with a W filament thermionic source from JEOL was employed for the analysis. The sample was prepared by drop-casting 1:100 diluted LDH dispersions (approximately 0.001 g/L) in ethanol onto ultrathin C-on-holey C-coated copper grids provided by Ted Pella.

- ThermoGravimetry-Differential Thermal Analysis (TG-DTA): the analyses were conducted using a LabsysEvo 1600–Setaram thermobalance. Approximately 20 mg of the sample was loaded into an open alumina crucible and subjected to heating from 30 °C to 1250 °C at a rate of 10 °C/min, under both argon and dry air atmospheres (60 mL/min).

- Total surface area calculation via Brunauer–Emmett–Teller (BET) theory: N_2 physisorption at 77 K was performed with a *Micrometrics ASAP 2020 MP*.

- Direct current (DC) magnetometry measurements were performed using a Physical Property Measurement System (PPMS) from Quantum Design, equipped

with a vibrating sample magnetometry (VSM) option. The sample material was already filled into polypropylene (pp) sample capsules (P125E from Quantum Design) Magnetic moment vs. temperature scans was measured from 2 to 300 K at a field of 0.5 and 5 kOe, respectively, in zero-field cooled (ZFC) and field-cooled (FC) mode. From 2 to 50 K the temperature was set in 'settle mode' and from 51 to 300 K in 'sweep mode' with a heating rate of 2 K/min. A measurement of magnetic moment was performed with a temperature step size of 1 K with an averaging time of 10 s. Magnetic moment vs. magnetic field scans were measured at 2 and 300 K in FC mode as full loop measurements with a maximum magnetic field of 70 kOe. At each field two measurements were performed, each with an average time of 10 s.

- The catalytic tests were performed in a lab scale pilot plant: circa 0.01 g of catalyst diluted with 0.25 g of silica sand to produce a fixed bed reactor (FBR) in a quartz tube (internal diameter 6 mm; length 0.5 cm). The flow of N_2, CO_2 and CH_4 (reactants mixture) could be controlled by three mass flow (*Bronkhorst EL-FLOW Select*) and the products gasses could be measured with a bubble flowmeter and an Agilent 7820A gas-chromatograph with TCD detector. Before the test the catalyst was reduced *in situ* in a stream of 15 mL/min of pure hydrogen at 673 K for 30 min. The catalytic assessment was carried out using a reactant mixture at a flow rate of 125 mL/min, with a composition of N_2: CO_2: CH_4 in a 2:2:1 ratio, within a temperature range spanning from 673 K to 873 K. A CH_4/CO_2 feed ratio of 0.5, deliberately selected below the stoichiometric value (1), was employed to enhance the system's resistance to carbon formation *(66)*. The mathematical demonstration to find the % of each product could be found appendix (chapter 4.1).

2.1.4. Cell preparation and electrochemical tests

The synthesized material can't directly be used in an electrochemical cell but must be prepared and assembled as an electrode. 70 % LDH was crushed in a quartz mortar for 10 min with a 20 % Conductive carbon, then was add as binder a 10 % of sodium alginate in a water/isopropanol (9:1) solution.

The so obtained ink was then coated on a 10 μm thick copper foil current collector, with a wet thickness of ~ 150 μm and dried in oven at 80 °C overnight, finally it was cut in discs of 12 mm diameter.

Each disc was then pressed at 8 ton, dried under vacuum at 120 °C and stored in the glovebox.

Sodium alginate is not a conventional binder, but previous studies demonstrate that is very suitable for LDHs*(50)*, it forms hydrogen bonds with the hydroxyl groups of the LDH, preventing undesired pealing and electrode cracklings and making the material more resistant to discharge/charge cycles.

Furthermore, sodium alginate is a natural polymer that could be prepared in aqueous solution without any solvents, making it more sustainable that the standard battery binder polyvinylidene fluoride (PVDF).

The electrodes, both for lithium and sodium batteries, were than tested in Swagelock ® T-Cells. The experiments, being a preliminary study, were carried out in a half-cell configuration to obtain all the possible information on the anodes in the best condition. The cells were assembled in an argon filled glovebox and consisted of the previously prepared electrode, a metallic lithium/sodium counter electrode and a metallic needle of lithium/sodium as reference electrode, the different parts were separated by a glass fibre partition. The chosen electrolytes were for LIBs the commercial LP30 (1 M $LiPF_6$ in ethylene carbonate/dimethyl carbonate in a weight ratio of 1:1) while for SIBs a 1M solution of $NaClO_4$ in ethylene carbonate/dimethyl carbonate (1:1) and 5 % wt fluoroethylene carbonate.

A schematic view of the electrochemical cells is presented in figure 6.

All the tests were performed in the potential range from 0.01 to 3 V vs Li/Li^+ or vs Na/Na^+ in a binder climate chamber at 25 °C by means of a multichannel potentiostat (VMP3, Bio-Logic). The experimental technique used were cyclic voltammetry (CV) at different

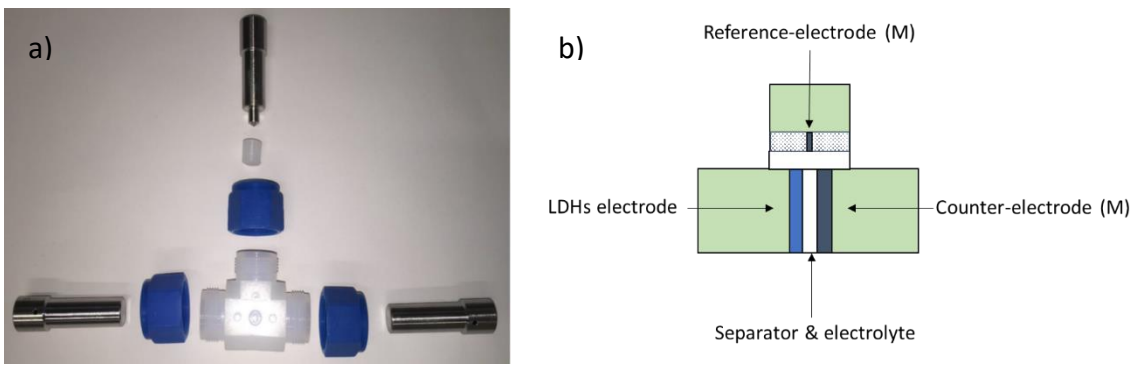

Figure 6: an open Swagelock® T-Cells a) and schematic description of a closed cell b).

scan rates raising from 0.01 mV/s to 10 mV/s, galvanostatic cycling with potential limitation (GCPL) at a current applied of 50 or 500 mA/g, and rate capability (RC) tests with an increasing applied current from 50 mA/g to 10A/g.

To allow *in-operando* X-ray Absorption Spectroscopy (XAS) measurements were also prepared special CR2032 coin cells consisting of the as-prepared working electrode, a sodium foil counter a glass fiber separator (Whatman glass microfiber filter, 675 μm thickness), and electrolyte (1 M solution of $NaClO_4$ in ethylene carbonate/dimethyl carbonate 1:1 and 5 % wt fluoroethylene carbonate).

X-ray absorption near-edge structure (XANES) and extended X-ray absorption fine structure (EXAFS) spectra for the Ni and Fe K-edge of samples with varying states of charge were obtained at the P65 beamline, PETRA III, German Electron Synchrotron in Hamburg (DESY). The XAS spectra were acquired at the Ni or Fe K-edge in transmission geometry using continuous scan mode. The double-crystal fixed-exit monochromator was outfitted with Si (111) crystals.

2.2. Application in LIBs

In this work were tested different LDHs, some specifically synthesized for electrochemical purposes, some others prepared for other purposes by the research group.

2.2.1. Preliminary tests

Several LDHs were tested as electrodes in Li ion half cells, all of them were subjected to a GCPL with an applied current of 50 mA/g. In figure 7 are reported their behavior in the first 50 cycles of charge-discharge. All materials show a high specific capacity in the first lithiation, then undergoing a marked ICL. Only NiAl-NO_3, NiFe-NO_3 and NiCo-NO_3 retain an acceptable value in the following cycles. Among them only the first two seem to be stable in cycling, furthermore cobalt is an element to be avoided for both environmental ad conflict-free concerning, so the first two compounds were selected for more in-depth studies.

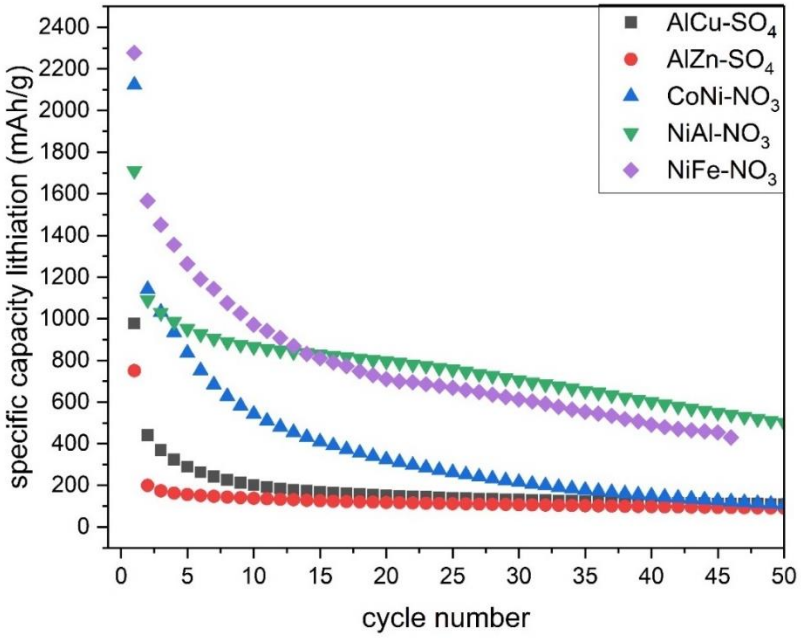

Figure 7: specific capacity in lithiation vs cycle number for different LDHs.

2.2.2. NiFe-NO_3 and its calcinated compounds

The material was completely characterized, the ratio between the metals was confirmed to be 2:1 by ICP-OES analysis, as shown in table 2.

Table2: amount of Ni and Fe in the LDH sample resulting from ICP-OES analysis.

	Amount of element (Mass %)	Amount of element (mol)	Atomic ratio
Ni	17	0.30	1.00
Fe	35.8	0.61	2.00

The FT-IR spectrum (figure 8a) shows only few signals; the broad and deep band centered at 3400 cm^{-1} is due to the O–H stretching of the hydroxides and intercalated water molecules, the signal of medium intensity at 1640 cm^{-1} is attributable to the bending mode of water and finally an absorption at 1380 cm^{-1} is related to the ν_3 vibration of nitrate *(50)*. The diffraction pattern of NiFe-NO_3 (figure 8b) confirms that the structure is the typical hexagonal LDHs one (space group R -3 m) *(67)*, the cell parameters calculated by means of WinPLOTR suite*(65)* are: a = 3.0(8) Å and c = 23.4(9) Å. All the reflections are broad underlining the small crystallites size and the low crystallinity of the compound, the peaks are the symmetric 003; 006; 009; 110; 113 and asymmetric 012; 015; 018 *(26,63,67–69)*. The asymmetric peaks are typical of turbostratic compounds, whose different basal planes have slipped out of alignment. That characteristic is also appreciable from the FE-SEM images at low magnification (figure 8c) revealing that the different sheets of material are staked in a random orientation. Furthermore, in the picture at high magnification (figure 8d) could be seen the nano structuring of the material surface.

On the compound was also performed a TG-DTA analysis in the temperature range 30 to 1250 °C underlaying the presence of three main mass losses (fig.9a).

The first one is between 30 and 250 °C and leads to a 14 % mass decreasing and could be attributable to the elimination of the crystallisation water and the subsequent disordering of the layered structure, after, between 250 and 360°C, is present a 10 % mass loss and from 360 to 500 °C a final 7 % mass lowering. The two last mass changes could be attributable to the dihydroxylation of LDH and degradation of interlayered nitrate.

Between 500 °C to 560 °C is seeable from the DTA curve an exothermic process without mass change, typical of recrystallization.

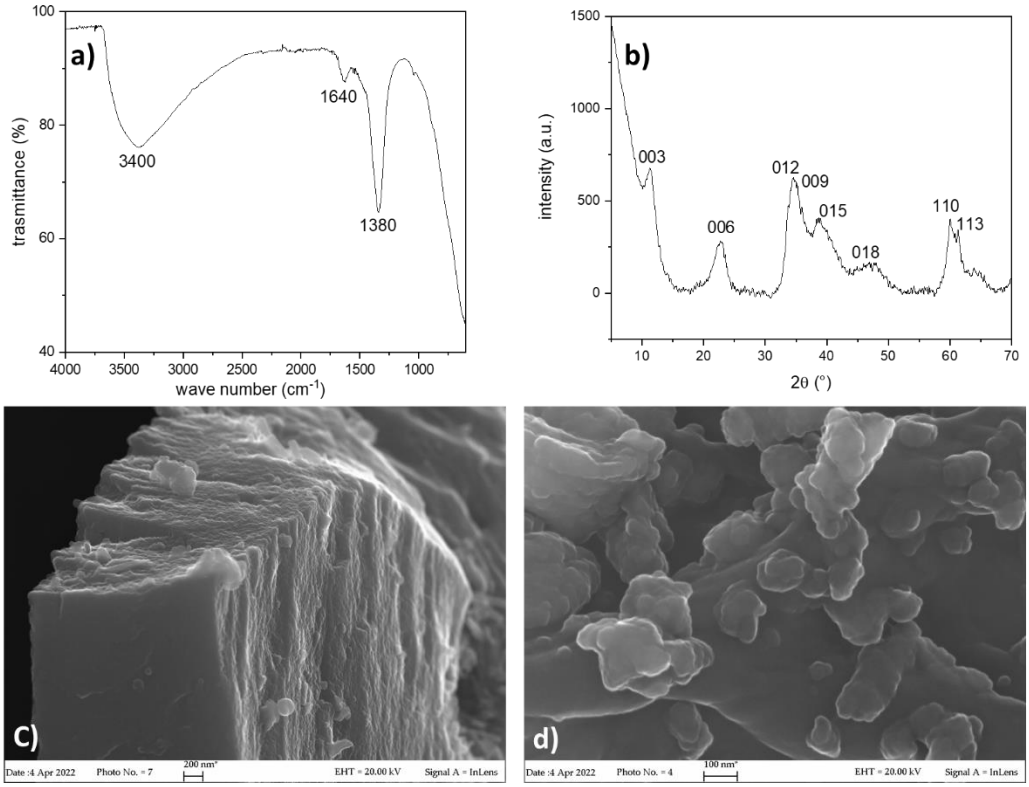

Figure 8: Figure 8: PXRD pattern (a), FT-IR spectra (b) and FE-SEM images at low (c) and high (d) magnification of NiFe-NO_3

To confirm those hypotheses, according to the TG data, were also prepared, from the initial material, three different samples annealed at 250, 360 and 560 °C from now NiFe-250, NiFe-360, NiFe-560). The samples were characterised via PXRD and FE-SEM. Figure 9b) compares the diffraction patterns of the different annealed samples: NiFe-250 displays a structure like the initial LDH, the enlargement of the reflections and the lowering in the intensity indicate an increase of disorder. At 360 °C, all the previous peaks disappeared and are presents only few large signals relatable to a mixture of disordered

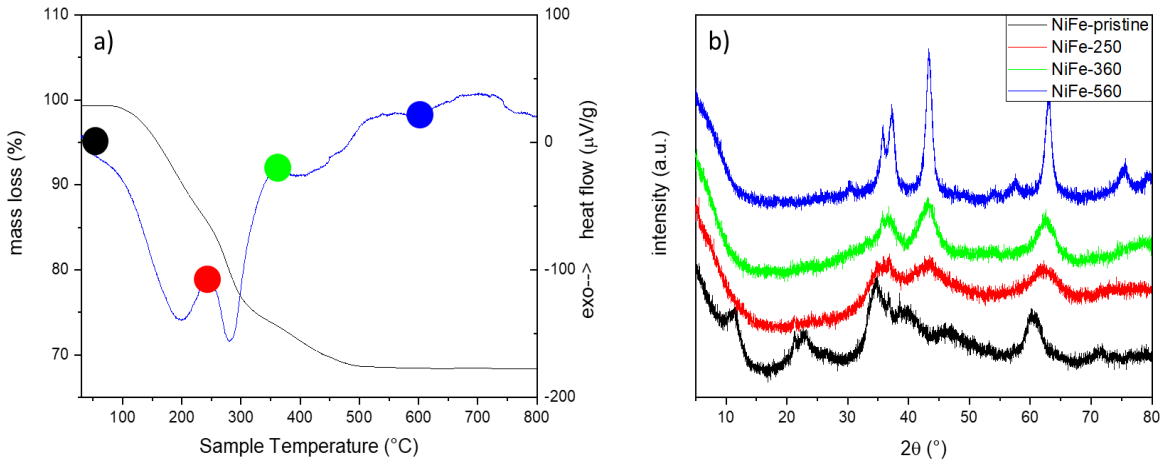

Figure 9: TG-DTA curve a) and PXRD pattern of NiFe-NO_3 and its calcinated compounds b): black is the pristine material red is NiFe-250, green is NiFe-360 and blue NiFe-560

Ni and Fe oxides. NiFe-560 shows the presence of well-defined and intense peaks attributable to the cubic phases Fe_2NiO_4 (spinel-like) and NiO.

This last process is also appreciable in fig. 10 where the FE-SEM image of NiFe-560 shows the presence of acicular crystals (typical of spinels).

The above-described steps are summarized in the following equations (eq.8 - eq.10):

$$[(Ni^{2+}_{0.66}Fe^{3+}_{0.33}(OH)_2]^{0.33+}[(NO_3)^-_{0,33}]^{0.33-} \cdot nH_2O \rightarrow$$
$$\rightarrow [(Ni^{2+}_{0.66}Fe^{3+}_{0.33}(OH)_2]^{0.33+}[(NO_3)^-_{0,33}]^{0.33-} + nH_2O_{(gas)} \quad (eq.8)$$

$$[(Ni^{2+}_{0.66}Fe^{3+}_{0.33}(OH)_2]^{0.33+}[(NO_3)^-_{0,33}]^{0.33-} \rightarrow$$
$$\rightarrow H_2O_{(gas)} + O_{2(gas)} + NO_{2\,(gas)} + Fe_2O_3 + NiO \quad (eq.9)$$

$$Fe_2O_3 + NiO \rightarrow Fe_2NiO_4 \quad (eq.10)$$

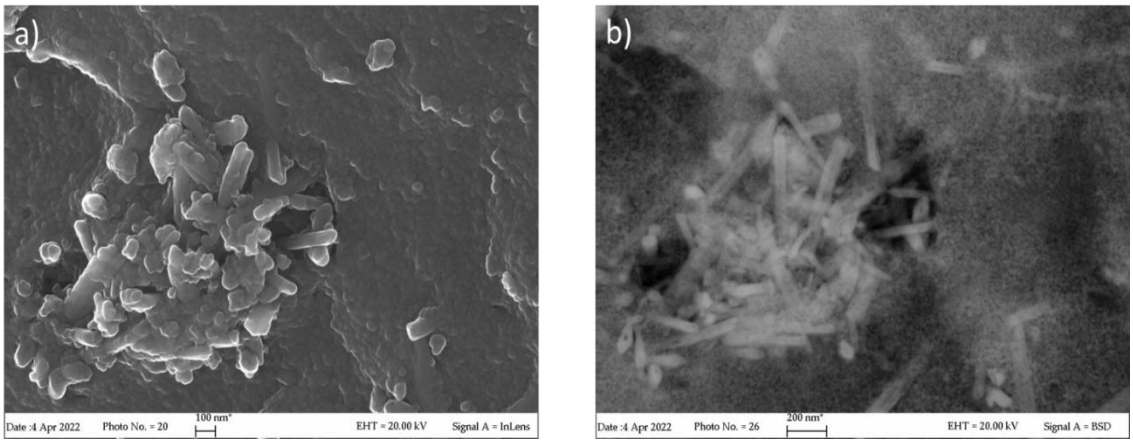

Figure 10: FE-SEM pictures of NiFe-560 recorded in lens a) and with the back scattered detector (BSD) b)

The pristine material and all the calcinated samples were prepared as electrodes and tested in lithium half cells as described in paragraph *2.1.4.*

On all the samples were CV with a scan rate of 0.1 mV/s and a GCPL at an applied current of 50 mA/g.

In all the four samples (fig. 11) the CV plot shows, for the first cycle, a different pattern compared to the subsequent one, this difference might depend on some irreversible reactions that lead to the activation of the material and the formation of the solid electrolyte interface (SEI). All the electrodes present some shared peaks: in lithiation a small and broad peak at around 1.5 V and a deeper one at 0.6 V, in delithiation the commons peaks are located at 1.7 V and 2.5 V. In the sample not treated (NiFe-pristine), as shown in fig. 11 a), in lithiation is present also a peak at 1 V and in delithiation at 1.1 V. These two peaks still appear, as shoulders that decrease their intensity, from NiFe-250 (fig. 11b) to NiFe-360 (fig. 11c) and completely disappear in NiFe-560 (fig. 11d).

In the following cycles all the samples show a sharp peak in lithiation at 0.9 V and in delithiation still at 1.7 V and 2.5 V. Even in this case NiFe-pristine shows more peaks; in lithiation at 1.6 V and at 0.5 V, in delithiation at 1.1 V. These are retained also in the other

samples, but they reduce their intensity following the temperature increasing until disappearing in NiFe-560.

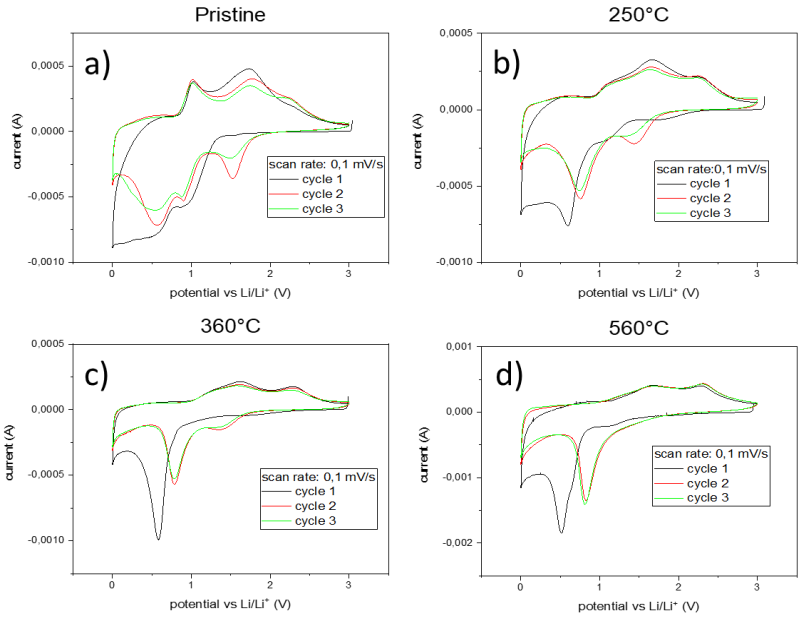

Figure 11: CV plot at 0.01 mV/s scan rate of NiFe-pristine a), NiFe-250 b), NiFe-320 c) and NiFe-560 d)

The common peaks, as well known in literature*(50,70,71)*, are pertaining to the conversion reaction of Ni, while the extra peaks seem to be related to some reactions that happen at the interlayer (like intercalation) since they lower their intensity with the decreasing of the layered structure.

From the GCPL plot (fig. 12) all the samples present a quite high irreversible capacity loss (in the order of the 30 % of the initial capacity) the shape of the curve is similar in all the samples; in discharge is present a long and tilted plateaux around 1 V followed by a more inclined one staring at around 0.5 V. In NiFe-pristine is present, at around 1.6 V, another tilted plateau that lowers its length in the other samples following the calcination temperature. All those data agree with the previous CV analysis.

From the cyclic stability plot (fig. 13a) it is clearly observable that NiFe-pristine needs some cycle to stabilise retaining around the 30 % of its initial capacity still delivering around 600 mAh/g.

Both NiFe-250 and NiFe-320 are not stable at all, the first has a linear continuous drop in capacity, the second displays a very quick one but after 40 cycles both retained only a 4 % of their initial capacity.

NiFe-560 is the more stable compound, after the first decreasing in the capacity the material stabilizes around a 50 % of the initial capacity delivering after 40 cycles 750 mAh/g. The coulombic efficiency plot (fig. 13b) confirms this trend: NiFe-pristine after

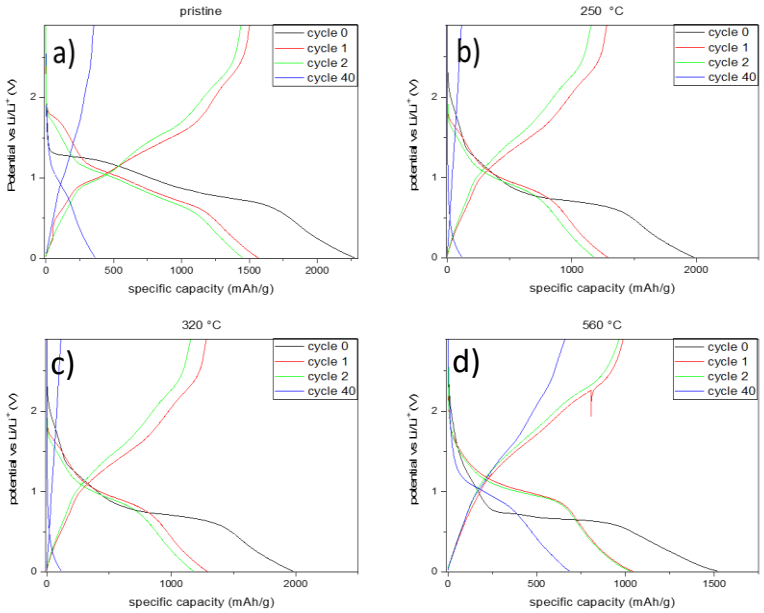

Figure 12: GCPL plot with an applied current of 50 mA/g of NiFe-pristine a), NiFe-250 b), NiFe-320 c) and NiFe-560 d)

few cycles and NiFe-560 almost immediately, stabilise maintaining an efficiency value of about 98 % while the other two samples have a very random behaviour and a great reduction in the capacity value (even less than the 75 %).

These results are very interesting in fact the final specific capacity of NiFe-pristine is not so different from the one of the NiFe-560 (that is almost only NiO, a material just well described in literature for its applicability in LIBs *(70,72)*.) having, just ¼ of nikel in terms of mass. This could be justified assuming a double mechanism of reaction that combine a conversion and an intercalation reaction, but further analysis are required to demonstrate this conclusion.

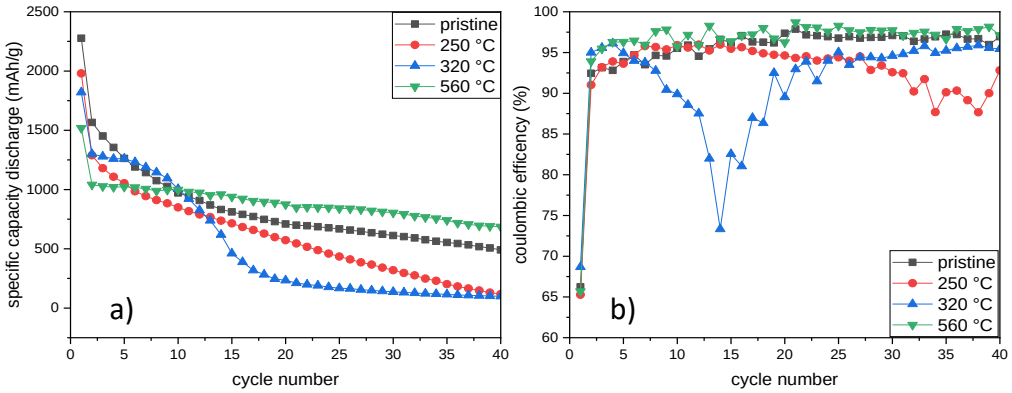

Figure 13: specific capacity in discharge vs cycle number (a) coulombic efficiency vs cycle number (b) of NiFe-pristine (black), NiFe-250 (red) NiFe-320 (blue) and NiFe-560 (green)

2.3. Application in SIBs

Basing on the obtained results in LIBs, it was decided to investigate the applicability of the most performing LDHs also in sodium ion batteries.

2.3.1. NiAl-NO_3

This material, respect to other samples obtained with different methods, is quite crystalline, and could be attributed to the hexagonal space group $R\bar{3}m$. (fig. 14a) The broad reflection (006) could be attributable to the phase separation with the same rhombohedral $R\bar{3}m$ space group. The calculated lattice parameters are a = 0.3015 nm; c = 2.3115 nm.

The value of $d_{(003)}$ approximately represents the space occupied by a NiAl octahedron and the interlayer region (basal spacing) *(73)*. The calculated *d* values is $d_{(003)}$ NiAl-NO_3 = 0.7607 nm and the interlayer dimension calculated as proposed by Conterosito *(74)* is about 0.28 nm.

The FT-IR spectra (fig. 14b) shows a broad absorption band at 3410 cm^{-1} attributable to the O–H stretching vibrations of the hydroxyl groups and structural water molecules *(75)*. The weak peak at 1632 cm^{-1} is addressable to the in-plane bending mode of water molecules. The sharp absorption band at 1348 cm^{-1} corresponds to the stretching vibration of NO_3^-, which confirms the presence of NO_3^- in the interlayer. The signals at 749 and 652 cm^{-1} are linkable to the stretching and bending modes of Al-OH and Ni-OH.

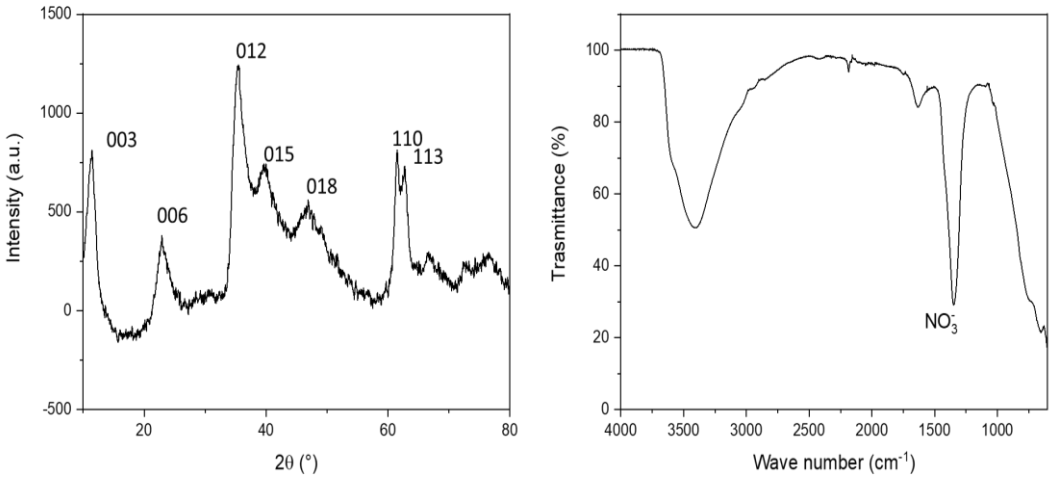

Figure 14: PXRD pattern a) and FT-IR spectra b) of NiAl-NO_3 LDH.

The FE-SEM images (fig. 15) show the morphology of NiAl LDH. The powder is constituted of a homogeneously dispersed lamellar clusters of 10/30 μm diameter (fig. 15a), increasing the magnification is possible to appreciate the flower-like structure (fig. 15b), the lamellae thickness range approximately between 20 and 40 nm.

This material was used to prepare electrodes and tested in Swagelock® T-cells as described in chapter *2.1.4*

It was performed a cyclic voltammetry on the material in at different scan rate, from 0.1 mV/s to 10 mV/s.

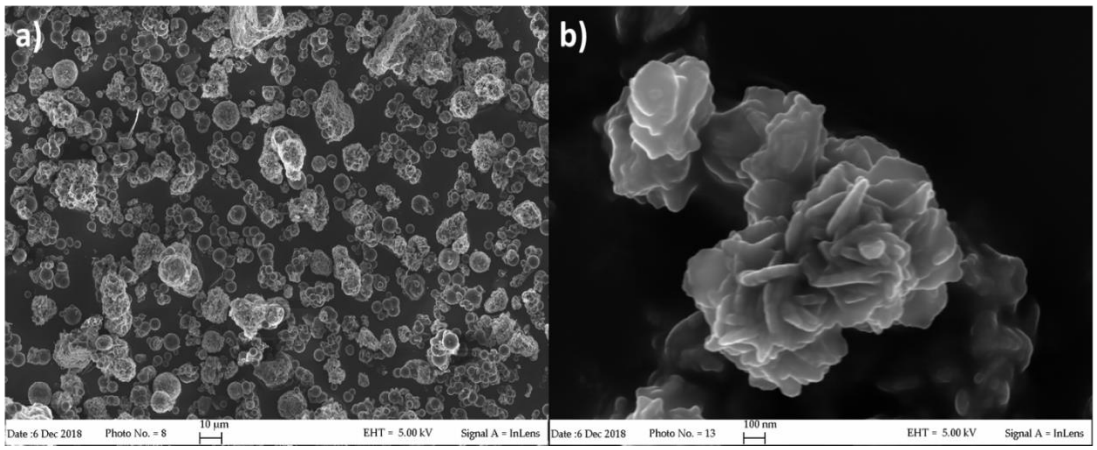

Figure 15: FE-SEM photos at low a) and high magnification b) of NiAl-NO_3 LDH.

As shown in figure 16a) The first sodiation presents a small peak at 1.1 V and a deep one at almost 0.4 V, in next reductions the 1.1 V peak disappear suggesting that it is linkable with some irreversible reaction, like the formation of the Solid Electrolyte Interface (SEI). The other peak moves to higher values (0.7 V indicating a decrease of polarization with a subsequent decreasing of resistance) and becomes smaller indicating that the first cycle was made up of both reversible and irreversible reactions. In oxidation are present two broad peaks at 1.2 V and 1.6 V since the first cycle and are retained in the following. At higher scan rates (fig. 16b), the peaks are retained but they become broader and shift to a lower value in reduction and higher in oxidation underlying an increase in polarization. Summarising seems that is present only one reaction in reduction and two in oxidation.

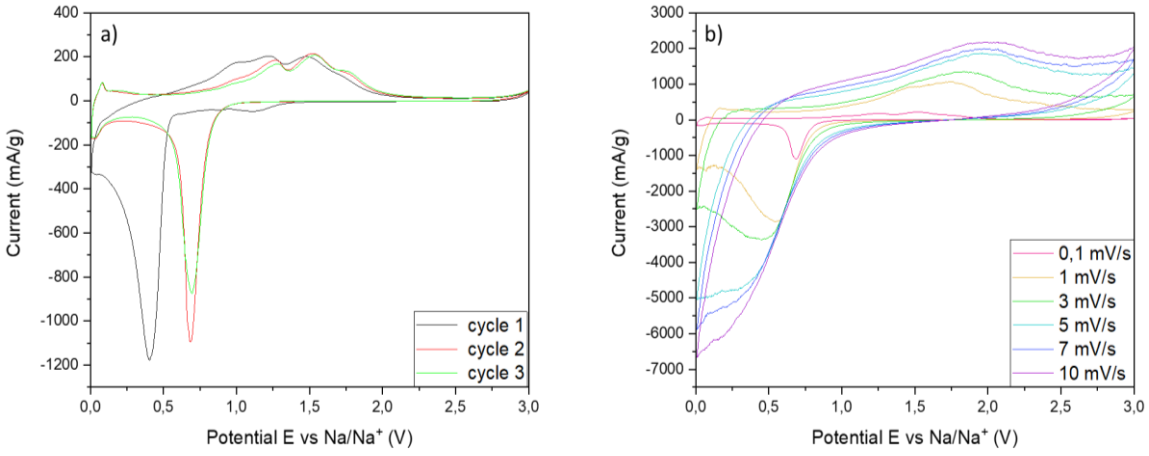

Figure 16: CV plot of NiAl-NO_3 in the potential range 0.01-3 V vs Na/Na^+ at 0.1 mV/s scan rate a) and increasing scan rate b)

From the experimental data were calculate the percentages of contribution, to the total specific capacity, of the outer and inner process with the Trasatti method*(76)*, the physical explanation of this method is presented in appendix 4.2. From those assumption was demonstrated that the involved reactions are almost only driven by diffusion as shown in figure 17.

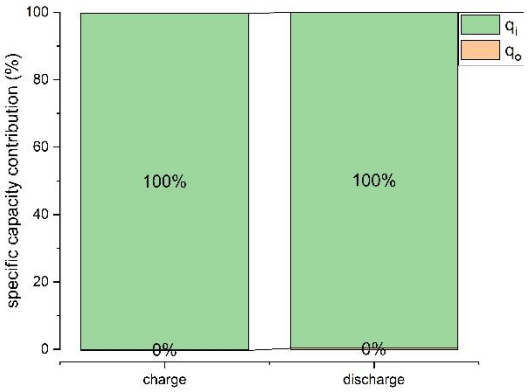

Figure 17: inner (q_i) and outer (q_o)contribution to the total capacity

It was also performed a GCPL test at 50 mA/g (fig. 18a). The first discharge shows an extremely high specific capacity ~ 1000 mAh/g and the curve shape is made of a first tilted plateaux at ~ 1 V and a second longer plateau between 0.6 and 0.4 V in agreement with the CV data. In the second discharge it is retained just the 52 % of the initial specific capacity and after 50 cycles for NiAl is retained only the 16 %, the curve plot after the first cycle shows 2 overlapped tilted plateaux between 1 V and 0.3 V in sodiation and of 2 contributions between 1.2 V and 1.8 V in oxidation in agreement with the CV plot.

The rapid specific capacity loss is even more clear from the specific capacity discharged vs cycle number plot (fig 18 b), after 5 cycles is present a big drop that led to very low specific capacity values (about 200 mAh/g), also the coulombic efficiency stays at a value of 95 % for all the 50 cycles indicating a not stable material.

The test was repeated with an applied current of 500 mA/g for 500 cycles (fig. 18c) the curve presents a similar shape respect to the previous one, the initial discharged specific capacity is > 1200 mAh/g, followed by a more prominent drop (50 % retention) and after 500 cycles only the 4 % of the initial capacity is retained. The coulombic efficiency takes ~ 50 cycles to stabilize at value near the 98 % when almost all the initial capacity was expired as shown in figure 18d).

The initial capacity loss can be explained by some reactions connected with the activation of the material and the formation of the SEI as expected by conversion reaction materials *(17,77,78)*. The material probably behaves initially as in LIBs with the initial intercalation an than conversion with the formation of metallic Ni*(50)*.

Also, the not stabilization could be explained by the volume change connected both with the Ni reoxidation to NiO and the intercalation of sodium that being larger than lithium is more difficult to accommodate leading to the cracking of the electrode and the subsequent continuous capacity loss.

Those stability issues make this material unsuitable for future possible applications, so it was not subjected to further analysis.

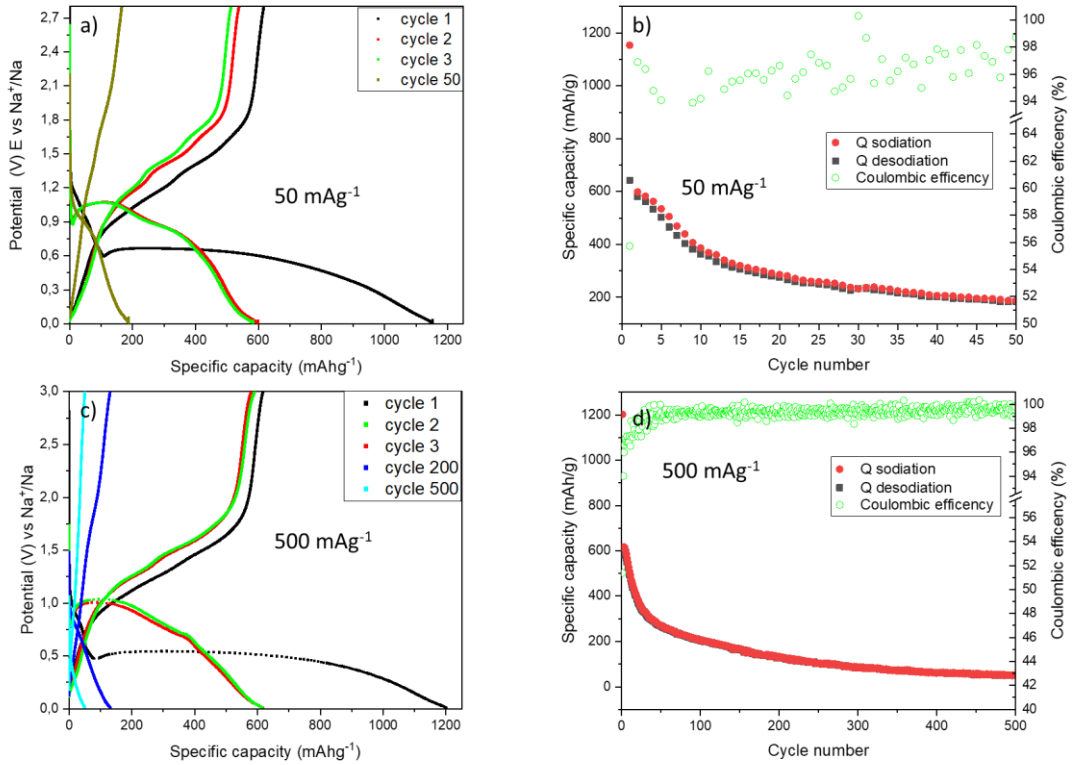

Figure 18: GCPL curves of NiAl-NO_3. Potential vs specific capacity a) specific capacity and coulombic efficiency vs cycle number b) with an applied current of 50 mAg^{-1} and Potential vs specific capacity c) specific capacity and coulombic efficiency vs cycle number d) with an applied current of 500 mAg^{-1}.

2.3.2. NiFe-NO_3

The previously described NiFe-NO_3 (*chapter 2.2.2.*) was also tested as anodic material in SIBs, the electrodes and cells were prepared as described in chapter *2.1.4.*
A CV of the LDH electrode vs. sodium metal was performed at different increasing scan rate 0.1 and 10 mV/s.
In figure 19a) are reported the first three cycles at low scan rate, in the first sodiation it is present a weak peak at 0.97 V attributable to the electrolyte degradation and formation of a solid electrolyte interface (SEI), ongoing toward higher potentials it is present a very broad asymmetric peak at 0.43 V related to the irreversible conversion reaction. Both the peaks disappeared in the sequent cycles and are substituted by two large peaks respectively at 0.75 V and 0.55 V, due to the reduction of Fe^{3+} *(79)* and Ni^{2+} *(71)*. In desodiation are present two main peaks at 0.75 V and 1.45 V pertaining to the reoxidation of Fe and Ni to a mixture of Fe/Ni oxides, these peaks are retained also in the following cycles*(71,79)*. Increasing the scan rate (fig. 19b) the compound undergoes polarization, but the above-described peaks are always retained.

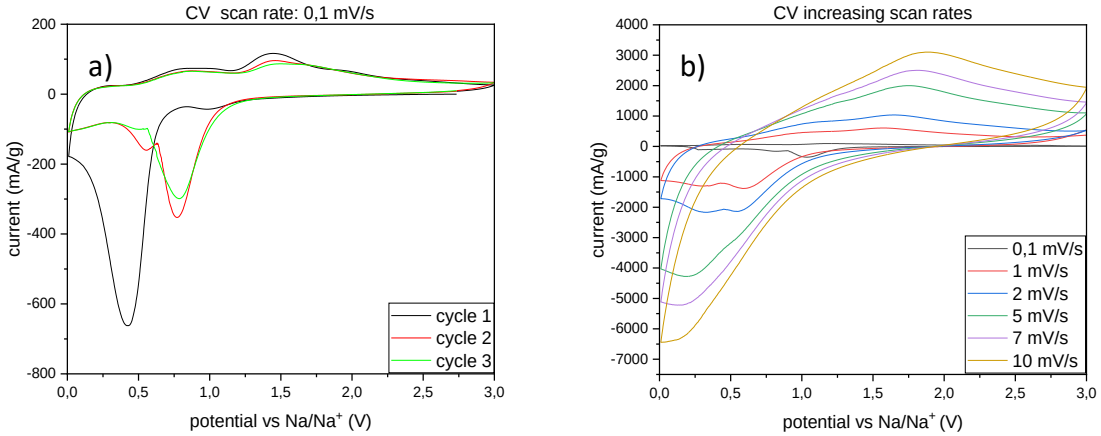

Figure 19: CV plot current vs potential. a) first three cycles at 0,1 mV/s scan rate. b) second cycle for each scan rate from 0,1 to 10 mV/s.

Those experimental data were also used to calculate the percentage of contribution to the total specific capacity of the outer and inner process with the Trasatti method (Appendix, chapter 4.2), demonstrating that the involved reactions are mainly driven by diffusion but there is also a ~ 15 % capacitance contribution (fig.20).

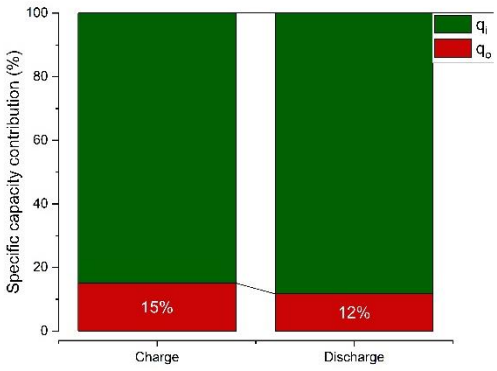

Figure 20: specific capacity contribution of inner (green) and outer(red) processes both in charge and discharge.

The galvanostatic curve of the NiFe LDH electrode, with an applied current of 50 mA/g is shown in figure 21a). In the first reduction is present a shoulder at about 1 V, then it is present a long-tilted plateaux between 0.8 V and 0.6 V immediately followed and partially overlapped with a more tilted one that end at 0.2 V, in agreement with what is observed in the CV plot. After the first cycle all contributions are replaced by a single plateau made of at least two contributions. In desodiation are appreciable two main contribution, that are retained in the following cycles, all those assumptions are also in agreement with the previously discussed CV data.

In the initial sodiation the specific capacity reaches 972 mAh/g and while during the first desodiation, it decreases to 579 mAh/g, so the coulombic efficiency registers a mere 60 % (fig. 21b), this could be related to irreversible reactions linked to partial electrolyte degradation, SEI formation, and material stabilization. As the cycles progress, capacity retention significantly improves, exceeding 95 % from the second cycle onwards. After 50 discharge/charge cycles, the material can still achieve 402 mAh/g in sodiation, indicative of a stable SEI and commendable cyclability.

Additionally, a galvanostatic cycling was conducted within the same potential range at 500 mA/g for 500 cycles (see figure 21c). The initial specific capacity in sodiation measures 760 mAh/g, contrasting with 420 mAh/g in desodiation. The initial coulombic efficiency is a mere 55 %, yet it markedly increases in subsequent cycles, stabilizing at approximately 98 % (see figure 21d). Even after 500 discharge/charge cycles, the material retains the ability to furnish 122 mAh/g.

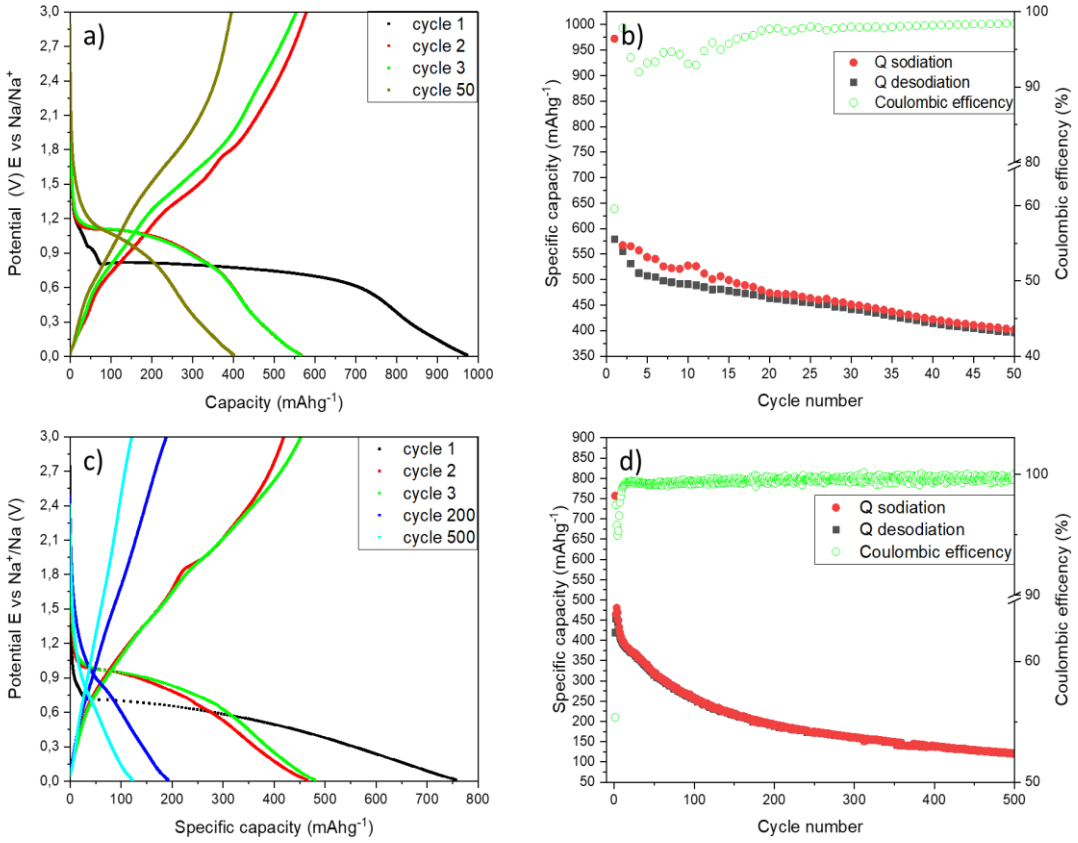

Figure 21: GCPL curves of NiFe-NO_3. Potential vs specific capacity a) specific capacity and coulombic efficiency vs cycle number b) with an applied current of 50 mAg^{-1} and Potential vs specific capacity c) specific capacity and coulombic efficiency vs cycle number d) with an applied current of 500 mAg^{-1}

To gain a more profound understanding of the stability of the material, an analysis of rate capability (RC) was conducted, involving a stepwise increase in current from 50 mA/g to 10 A/g. This assessment was carried out within the 0.01 to 3 V vs Na/Na^+ potential window (refer to figure 22). The initial 5 cycles (at 50 mA/g) closely resemble those observed in the GCPL under identical conditions. The specific capacity during the first sodiation is remarkably high at 945 mAh/g. However, a substantial irreversible capacity loss (ICL) occurs during the first desodiation, resulting in a 60 % retention of specific capacity. As the material stabilizes, the specific capacity delivered by the end of the fifth cycle is 475 mAh/g.

By increasing the applied current, the initial specific capacity experiences a decline, maintaining a relatively stable trend throughout the five cycles, characterized by a "stair-like" pattern. At an applied current of 10 A/g, the electrode can only deliver 45 mAh/g. Nevertheless, NiFe-LDH demonstrates that reverting to the initial applied current of 50 mA/g could once again yield a reversible capacity of 430 mAh/g.

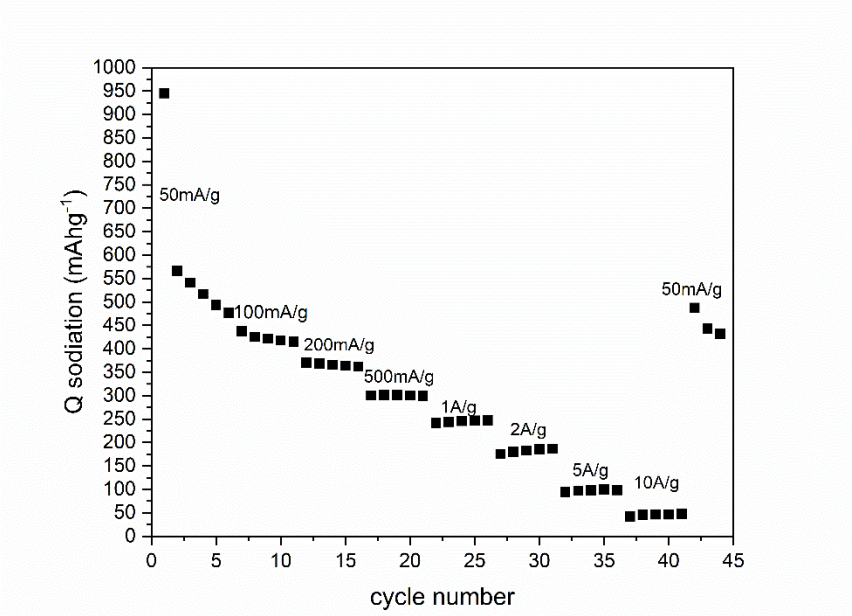

Figure 22: RC plot of NiFe-NO_3 at increasing applied currents, from 50 mA/g ti 10 A/g

To explain the high stability of the NiFe LDH was investigate the mechanisms occurring during the charge discharge processes. Being both Ni and Fe elements that could lead to a variety of compounds with characteristic magnetic behavior were perform some magnetic measurements on the pristine material and on the discharged (sodiated) and charged (desodiated) electrode. First, the purity of the pristine material was checked, in fact is well known that the Fe based LDH are susceptible to magnetite impurities not detectable by PXRD *(80)*.

As shown in appendix 4.3 figure A1 the zero-field-cooled (ZFC) and field-cooled (FC) susceptibility χ curves, acquired at 500 Oe and 5 kOe, overlay seamlessly from 300 K down to approximately 30 K. They manifest a Curie-Weiss behaviour with an inverse temperature dependence, characteristic of localized magnetic moments. Below the 30 K threshold, the ZFC/FC curves remain superimposed, but the susceptibility values at 5 kOe fall below those at 500 Oe, signifying a departure from pure paramagnetic behaviour with a linear correlation to the magnetic field. Distinct bifurcations in the ZFC and FC curves emerge, with the FC curves reaching a maximum at 9.0(5) K (500 Oe) and 6.0(5) K (5 kOe), indicative of ferrimagnetic ordering at these low temperatures.

From the FC curve at 5 kOe, the χT vs. T plot in figure 23 is derived, aiding in the confirmation of the oxidation states of Ni and Fe ions in NiFe-LDH. Assuming the sum formula $[Ni^{2+}_{0.66}Fe^{3+}_{0.33}(OH)_2]^{0.33+}[(NO_3)^{-}_{0.33}]^{0.33-}$ for NiFe-LDH, Ni^{2+} and Fe^{3+} ions contribute to the magnetic susceptibility. Ni^{2+} has an electronic configuration $[Ar]3d^8$, with a $(t)^6(e)^2$ orbital occupation (in octahedral coordination), resulting in a total spin S = 1 and a paramagnetic moment of 2.83 μB. Fe^{3+} has an electronic configuration $[Ar]3d^6$, with a $(t)^4(e)^2$ orbital occupation and total spin S = 5/2 (in high spin), yielding a paramagnetic moment of 5.92 μB. Given the presence of 0.66 Ni^{2+} and 0.33 Fe^{3+} per formula unit, the total paramagnetic moment is calculated to be 4.12 μB, corresponding

to a Curie constant of C_{calc} = 2.126 cm^3 K mol^{-1}. The proximity of this calculated value to the $\chi T = C$ value at high temperatures (fig. 23) confirms that Ni in NiFe-LDH is in the present as Ni^{2+} and Fe is present only as Fe^{3+}. The increasing χT with decreasing temperature suggests the presence of slight magnetic ordering even at elevated temperatures, deviating from a strictly constant Curie constant. All of this information are in good agreement for what is reported in literature*(80)* so the material could be considered pure.

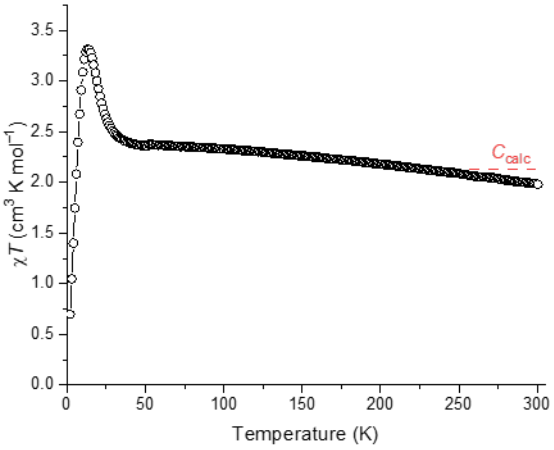

Figure 23: χT vs. temperature plot as obtained from the FC susceptibility curve measured at 5 kOe. The Curie constant C_{calc} as obtained if the Ni and the Fe would be present as Ni^{2+} and Fe^{3+} in NiFe-LDH is inserted as dashed line.

After that was decided to analyse *ex-situ* also the pristine electrode and the discharged and charged ones.

The carbon and binder added to the active NiFe-LDH material can be reasonably disregarded for magnetic measurements, as they merely contribute a faint diamagnetic signal. Figure A2 (appendix 4.3) illustrates that field scans of the pristine powder and the electrode with pristine powder coincide when considering only the mass of the active material in the electrode. In contrast, field scans for the pristine, discharged, and recharged NiFe-LDH material significantly differ from one another. As depicted in Figure 24, the field scans for the pristine material align with the susceptibility measurements discussed earlier. At 300 K, a pure linear magnetic moment-field behaviour, characteristic of a Langevin paramagnet with localized moments, is evident. At 2 K, the presence of magnetic order is confirmed by the observed hysteresis. The ferrimagnetic order, inferred from the reduced bifurcation temperature of the ZFC/FC with an increasing measuring field, also corresponds to the non-saturating behaviour, even at 7 Tesla.

Conversely, the discharged sample predominantly exhibits a field scan typical of a soft ferro/ferrimagnetic material, reaching a saturation magnetization of approximately 0.25 μB per formula unit at around 1 T at 300 K. The slight decrease in magnetization with an increasing field suggests diamagnetic contributions from closed shells also play a role in

the overall signal. In a hypothetical ferromagnetic phase with Ni^{2+} (spin S = 1) and Fe^{3+} (spin S = 5/2) contributing, a moment of about 3 µB would be expected, but the considerably lower observed saturation magnetization indicates the formation of a ferrimagnetic phase in the discharged sample, where magnetic moments partially cancel each other. No significant difference is observed in the field scan of the discharged sample at 2 K. For the recharged sample, magnetization slightly decreases with an increasing field, indicating a dominant diamagnetic contribution. This could be explained by the ordered magnetic moments of Ni and Fe ions in an antiferromagnetic phase, cancelling each other out, like the behaviour observed in NiO and nanosized α-Fe_2O_3*(81,82)*.

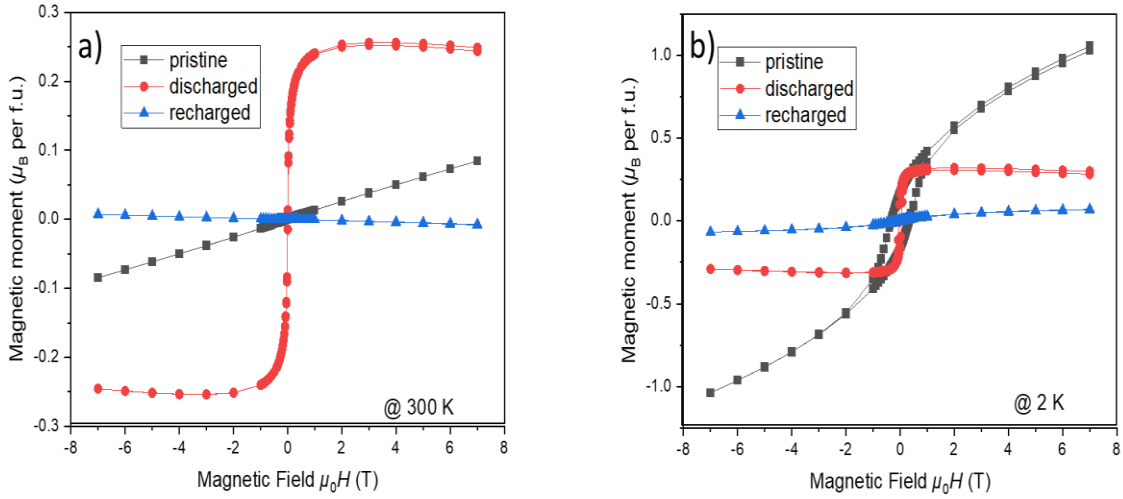

Figure 24: Magnetic moment vs. field plots for the pristine, discharged, and recharged NiFe-LDH as obtained from the electrode composite materials measured at a) 300 K and b) 2 K.

The NiFe-NO_3 based electrode was also subjected to *in operando* XAS analysis at the Hamburg synchrotron (DESY) to clarify its reaction mechanism. The spectra were recorded at different time to investigate several regions of the first discharge/charge cycle. The XANES (X-ray Absorption Near Edge Structure) spectra of the original NiFe-LDH compound reveal that the Ni and Fe oxidation states are +2 and +3, corresponding to the K-edge position of standard oxides. In sodiation, both cations experience reduction as depicted in the CV plot (fig. 19). Specifically, Fe^{3+} undergoes reduction to $Fe^{2+,}$ while Ni^{2+} is reduced to an intermediate state (fig. 25a; fig. 26a).

Analysis of the Fourier Transform (FT) for the Extended X-ray absorption fine structure (EXAFS) spectra from the in-operando experiment (fig. 25b, d; fig. 26b, d) indicates that the local structure of Ni undergoes minimal change compared to that of Fe. Post-sodation, a phase transition occurs with a deformation, characterized by a decrease in amplitude for the first and second coordination shells of Ni and Fe ions. Throughout this phase transition, bond lengths undergo continuous changes: Fe-O bonds lengthen, while the Fe-Fe (Fe-Ni) distance shortens. This shift is evident in the Fourier transform magnitudes of the first and second shells of Fe and Ni ions. In the Ni K-edge spectra, all FT magnitudes

shift slightly to lower R values, signifying small reductions in distances between Ni-O and Ni-Ni. Upon desodiation, the material does not revert to its initial NiFe-LDH structure. The local Ni structure remains close to the sodiation state (fig. 25c), whereas the local structure of Fe ions partially returns to the initial stage, confirming that the initial sodiation induces irreversible changes in the structure (fig. 26c).

It should be noted that in the compound the positions of Fe and Ni ions are connected by the oxygen Ni-O-Fe. As it was already recognized, this type of connection allows the influence of Fe ions on the oxidation state of Ni ions stabilising them at Ni (II)*(83)*.The theoretical specific capacity calculated for NiFe-NO_3 as a pure conversion material with Fe and Ni as redox centres is 477 mAh/g, this value is lower than the experimental one in first sodiation (976 mAh/g) where some irreversible reactions happen (SEI formation, material activation…) but is also lower to the value in the following cycles so probably is present also a contribution of the NO_3^-. Furthermore, from the XAS data is demonstrated that neither Ni nor Fe reaches the (0) oxidation state so the reaction mechanism seems much more complex than expected.Taking in account all the previous analysis the main reaction mechanism hypnotizable is in the first sodiation a transformation of the LDH structure that led to the formation of the ferrimagnetic Fe_3O_4 (partial reduction of Fe^{3+} to Fe^{2+}) and NiO that could be intercalated by sodium as Na_xNiO as reported by Verdianto*(84)*. In desodiation those compounds undergo a reoxidation to NiO and α-Fe_2O_3 that exhibit an antiferromagnetic behaviour. The mechanism, after the first cycleactivation, is a mixture of intercalation and conversion reactions and could be resumed in the following scheme (eq. 15):

$$\mathrm{NiFe-NO_3\ LDH} \rightarrow \mathrm{Fe_3O_4};\ \mathrm{Na_xNiO} \rightleftarrows \mathrm{NiO};\ \alpha-\mathrm{Fe_2O_3} \qquad (\mathrm{eq.}\ 15)$$

The presence of some other reversible reactions (involving NO_3^-) and different phases at this state of the resource could not be exclude.

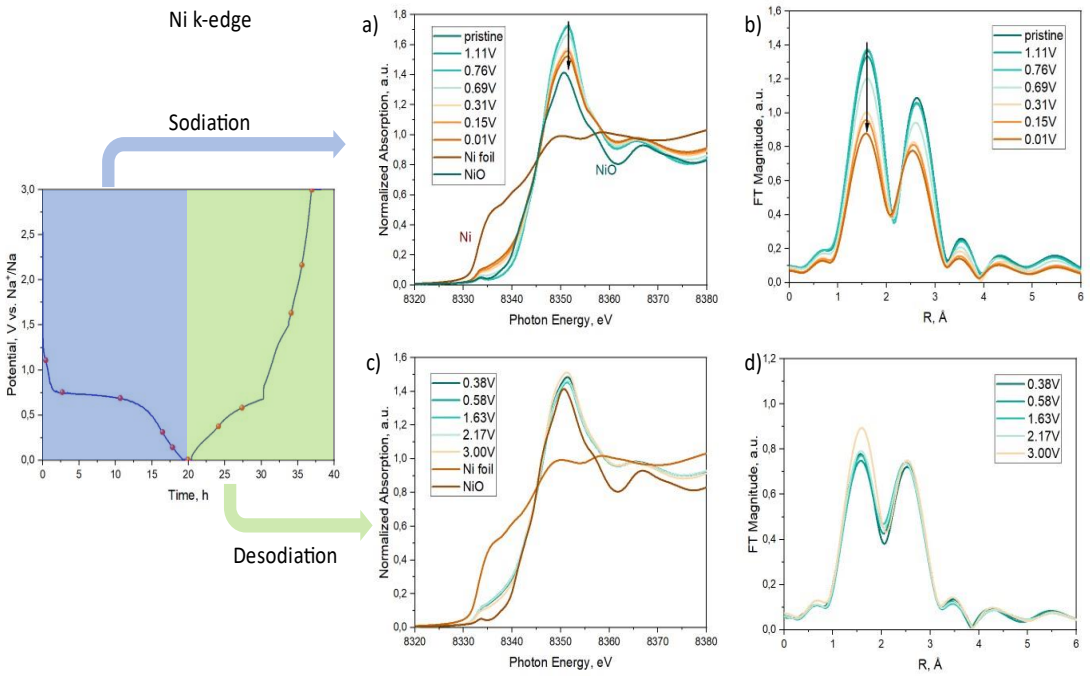

Figure 25: The normalized Ni K-edge XANES spectra (a, c) Fourier transform Ni K-edge EXAFS spectroscopy (b, d) of Ni foil, NiO standards and NiFe-LDH.

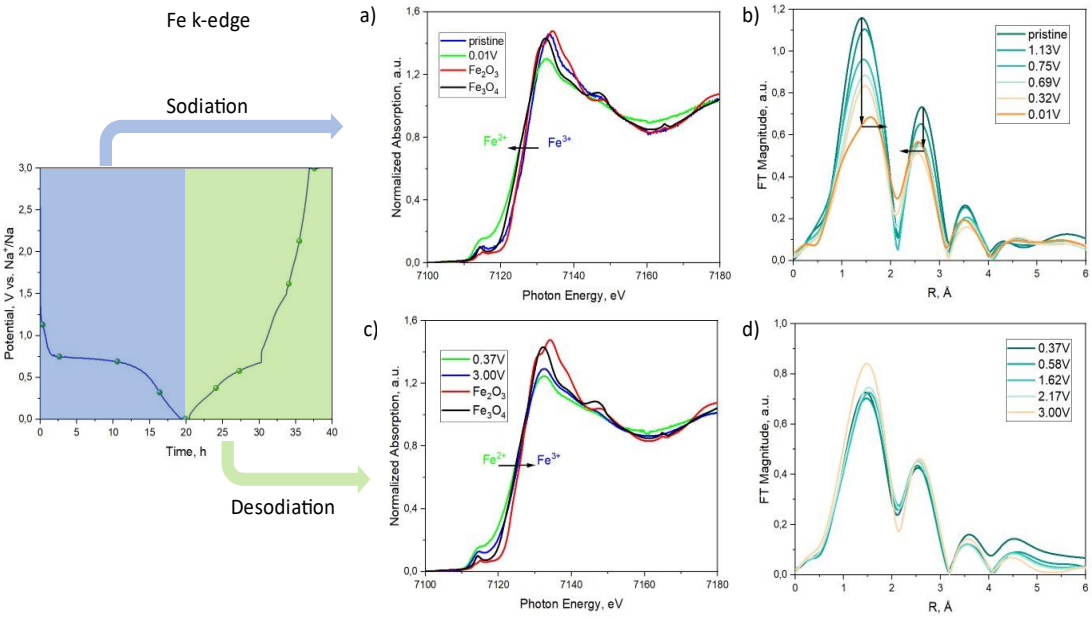

Figure 26: The normalized Fe K-edge XANES spectra (a, c) Fourier transform Fe K-edge EXAFS spectroscopy (b, d) of of Fe_2O_3, Fe_3O_4 standards and NiFe-LDH.

2.3.3. NiFe-CrO_4

Following those encouraging results was decided also to test a NiFe-NO_3 after the absorption of CrO_4^{2-} in the aim of a circular economy. The material comes from a project done in my research group, in collaboration with Dr. Francisco Ardini (DCCI-UNIGE), aimed at determining the best conditions to achieve the maximum absorption of the chromate. The material characterization was not part of this project but is present in appendix 4.4 for a better comprehension of the work.

NiFe-CrO_4 was treated as the other LDHs and prepared like an electrode as described in chapter 2.1.4.

The CV plot (fig. 27) shows a shape very similar to the NiFe-NO_3, but all the peaks are shifted to a lower potential.

After the first "activation" cycle NiFe-CrO_4 presents 2 more marked peaks respect to Ni Fe-NO_3 at 0.7 V in sodiation and 2 V in desodiation, this are attributable to the redox reaction Ni/Ni^{2+} wile all the other peaks are of similar intensity*(85)*.

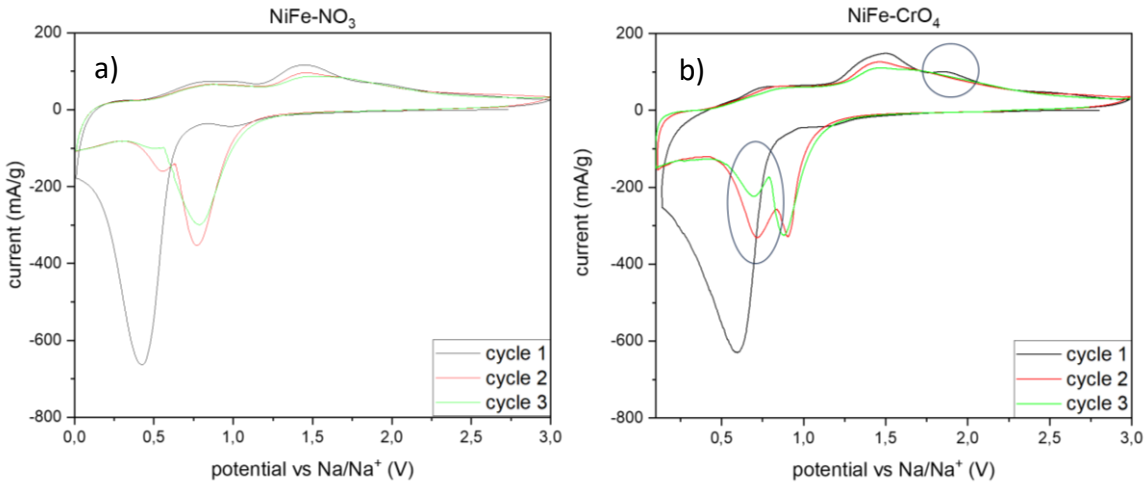

Figure 27: CV plot of the first 3 cycles at 0,1 mV/s scan rate of NiFe-NO_3 a) and NiFe-CrO_4 b). The blue circles underline the difference in the two plots.

GCPL plot (fig. 28) displays that in the first cycles the delivered specific capacity in discharge is very similar wile in recharge NiFe-NO_3 shows higher values, after 5 cycles the two trends start to diverge and NIFe-CrO_4 undergoes a rapid and continuous drop delivering after 50 cycles just 150 mAh/g against the 450 mAh/g of NiFe-NO_3.

This trend is very appreciable by the two CE where the difference in term of stability is disarming. The NiFe-CrO_4 never reach the 95 % indicating the presence of a lot of irreversible reactions while his counterpart in few cycles stabilise around 98 %.

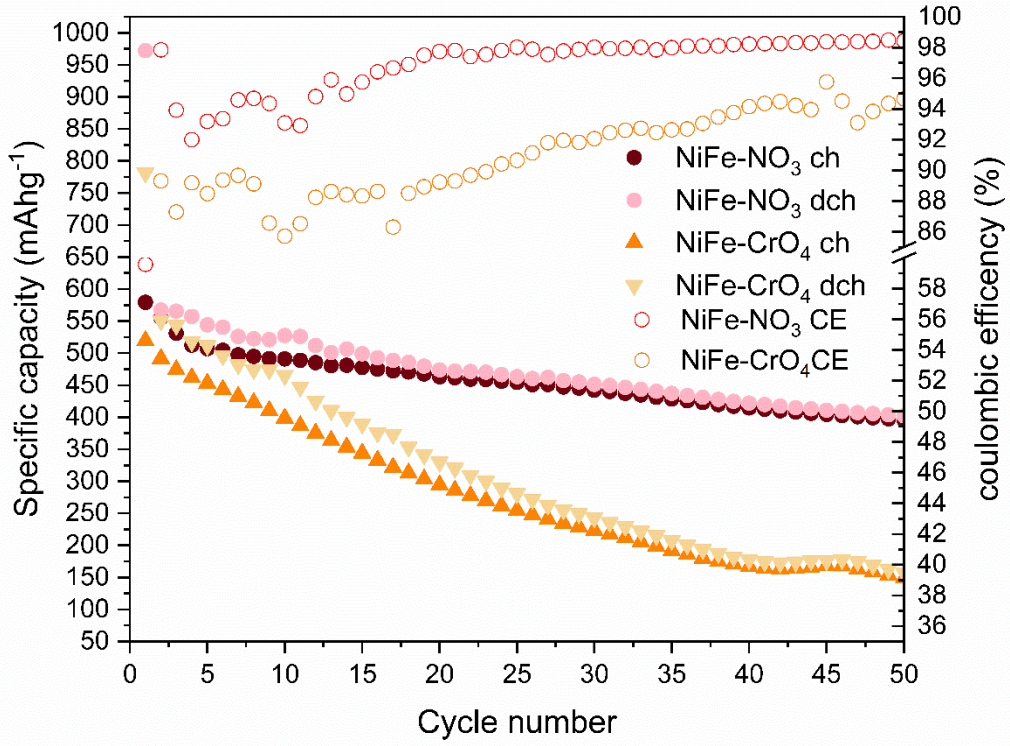

Figure 28: specific capacity vs cyle number and CE vs cycle number plots of NiFe-NO_3 (reds) and NiFe-CrO_4 (oranges)

In fact, NO_3^- was hypothesised as stabiliser of NiO; in reduction it sems to prevent the complete redox of Ni^{2+} to Ni^0 that involves a huge volume change stabilising the oxides and the above-described intercalation reactions (chapter 2.3.2)

2.4. Other applications

2.4.1. MgFe- Cl

An important application of LDHs is the anion exchange, specially, for what concern hazardous pollutants. Among them one of the most worrying is Cr (VI), owing to its mobility, solubility, bioaccumulation behavior and high carcinogenicity*(86–88)*. For this reason, was decided to study MgFe-Cl (MFC) as a material able to exchange the Cl^- (that has low affinity for the LDH interlayer) with the chromate.

The main problem to overcome in the preparation of the material is the contamination with other competitive anions especially the CO_3^{2-} so two different approaches have been attempted the direct coprecipitation synthesis and the reformation through "memory effect" (MFC-mem). Both materials where completely characterized and subjected also to a TG-DTA coupled with GC-MS to try to understand the difference in the composition in particular the relative amounts of CO_3^{2-} and Cl^-.

As depicted in figure 29, the diffraction patterns of MFC-1 and MFC-mem exhibit similarities, displaying the characteristic symmetric (003), (006), (110), (113) and asymmetric (009), (015), (018) reflections typical of MgFe-LDH, as documented in the literature *(89)*. Cell parameters were deduced from this data, yielding the following results: For MFC-1, a = 0.3122(3) nm, c = 2.3042(48) nm, V_{cell} = 0.1945(5) nm^3, and for MFC-mem, a = 0.3103(3) nm, c = 2.4641(60) nm, V_{cell} = 0.2055(6) nm^3.

In the diffraction pattern of MFC-1, a peak at 18° is observed, attributed to an excess of unreacted $Mg(OH)_2$. A comparison of the two PXRD patterns reveals a noticeable shift towards lower angles in the plot associated with MFC-mem, indicating a higher d value. The $d_{(003)}$ values, representing the space encompassing one Mg/Fe octahedral layer and the interlayer region (basal spacing), are calculated as $d_{(003)}$MFC-1 = 0.7634 nm and $d_{(003)}$ MFC-mem = 0.8160 nm, reflecting a difference of 6.5 %. With an estimated hydroxide layer thickness of approximately 0.24 nm *(74)*, the interlayer regions' thickness is estimated to be 0.52 nm and 0.58 nm for MFC-1 and MFC-mem, respectively.

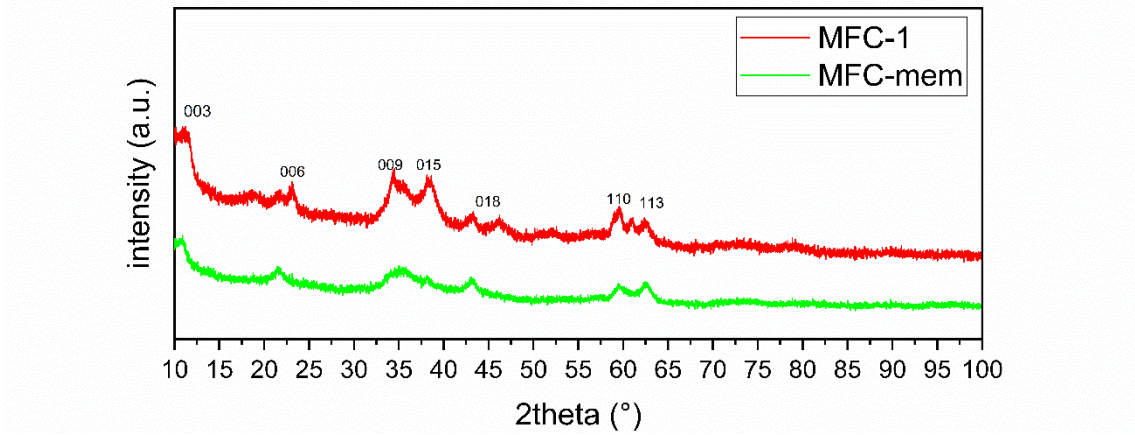

Figure 29: PXRD pattern of MFC-1 (red) and MFC-mem (red)

This discrepancy in interlayer size for the two compounds underscores the presence of a varied ratio of carbonate and chloride anions in the interlayer region. Furthermore, the broadness of the peaks distinctly indicates the nanometric size of the crystallites.

Figure 30 displays the FT-IR spectra of MFC-1, MFC-calc and MFC-mem, by comparison it becomes evident that the carbonate anion in these structures occupies two distinct sites, resulting in different bonding configurations. The carbonate anion is found in the interlayer and forms also a direct bond with a transition metal in the lattice, specifically iron in this case.

In the spectrum associated with MFC-1, a higher concentration of interlayered carbonate is observed. The absorption band, representing the vibrational modes of the symmetric interlayer carbonate, manifests as a single broad band at 1355 cm^{-1}, with a small shoulder at 1470 cm^{-1}. In MFC-calc, where all interlayered compounds were eliminated through heating, the spectrum shows nearly negligible signals in the carbonate region. The reaction proposed by Kanezaki at 180 °C involves the interlayer carbonate reacting with part of the crystal water (eq.16) and the only remaining carbonate signal in this spectrum is attributed to the anion coordinated with iron*(90)*.

$$CO_{3(\text{interlayer})}^{2-} + H_2O_{(\text{structural})} \rightarrow 2OH_{(\text{interlayer})}^{-} + CO_{2(\text{gas})} \qquad (\text{eq. } 16)$$

For MFC-mem, the carbonate signal is split into four smaller peaks at approximately 1530; 1500; 1400 and 1300 cm^{-1}. This splitting is attributed to the contributions of both interlayered carbonate (though less intense than in MFC-1) and directly bonded anion.

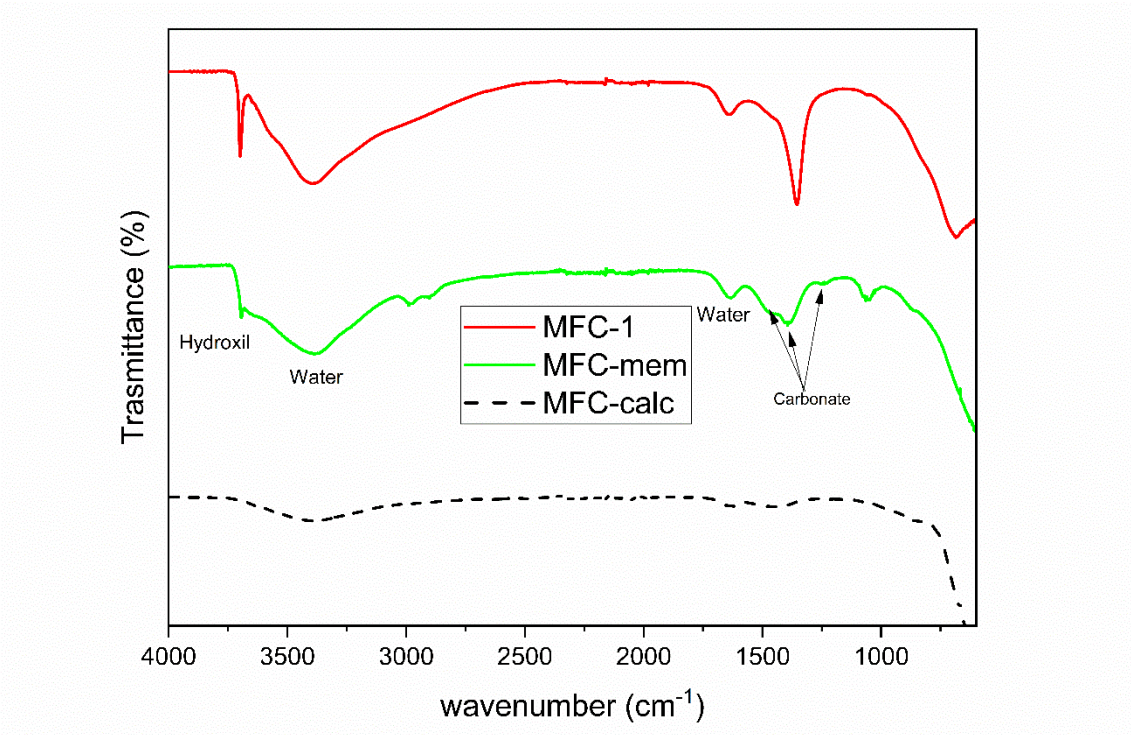

Figure 30: FT-IR spectra of MFC-1 (red) MFC-mem (green) and MFC-calc (dotted black)

As depicted in figure 31, both MFC-1 and MFC-mem exhibit mass loss occurring through four main steps. The initial two steps, spanning from 100 °C to approximately 330 °C, can be attributed to the release of water and CO_2, as confirmed by the GC–MS (fig.32).
The initial decrease in mass, commencing around 100 °C, aligns with the reaction outlined in eq. 16. The subsequent mass reduction, starting from 280 °C, is a result of the dehydration of hydroxides and the calcination of some directly bonded carbonate, as indicated by eq. 17 and eq. 18, respectively.

$$M(OH)_2 \xrightarrow{\Delta T} MO + H_2O_{(gas)} \qquad (eq.\,17)$$

$$MCO_3 \xrightarrow{\Delta T} MO + CO_{2(gas)} \qquad (eq.\,18)$$

In the case of MFC-1, the two processes conclude at 350 °C, resulting in a mass decrease of 23.0 %, while in MFC-mem, they conclude at 340 °C with a 20.3 % mass loss. At this point, the LDH structure is completely degraded in both samples. The termination points of the thermal effects for both analyses were determined based on the more pronounced endothermic peaks in the DTA curves.
Moving towards higher temperatures (from about 400 °C), another mass loss occurs, with a higher magnitude for MFC-1 compared to MFC-mem and is once again associated with the release of carbon dioxide as described by the GC-MS trace (fig. 32). The mass loss within the temperature range of 400 °C to 800 °C is 4 % higher for MFC-1 in comparison to MFC-mem. Interestingly, during the decomposition at temperatures below 400 °C, a substantial formation of formic acid (HCOOH) was detected for both compounds. Notably, this acid was not utilized in the LDH synthesis, suggesting its formation during thermal analysis through reactions between CO_2 and water, potentially catalysed by the LDH structure itself, as suggested in eq. 19.

$$2CO_2 + 2H_2O \xrightarrow{\Delta T-LDH} 2HCOOH + O_2 \qquad (eq.\,19)$$

The fourth stage occurring at a temperature exceeding 900 °C results in an additional mass loss, producing a substance undetected by the GC–MS device, possibly a volatile chlorinated salt at that temperature. This final step is more pronounced in MFC-mem than in MFC-1 and contributes to a total mass loss of 32 % in both samples. Throughout the entire thermal analysis of both LDHs, no chlorinated compounds were identified; only CO_2, water, and formic acid were observed. The presence of chlorine is expected to be investigated in the last mass step, involving the evolution of potential volatile salt that is not detectable by the GC–MS. This observation aligns with the higher magnitude of the last mass loss in MFC-mem.
The comprehensive analysis suggests that both synthesis pathways can't lead to the formation of a pure chlorinated LDH. While the memory effect-based synthesis appears to be more effective than simple coprecipitation, it still yields only a small proportion of the desired compound. Achieving pure MFC might require highly controlled conditions, such as within a glove-box, making this method somewhat more intricate and costly. The

GC–MS analysis conducted during the DTA/TG has indicated that the Mg-Fe LDH could potentially serve as a catalyst for the formation of formic acid (HCOOH) at low temperatures, especially when the oxides have not yet formed.

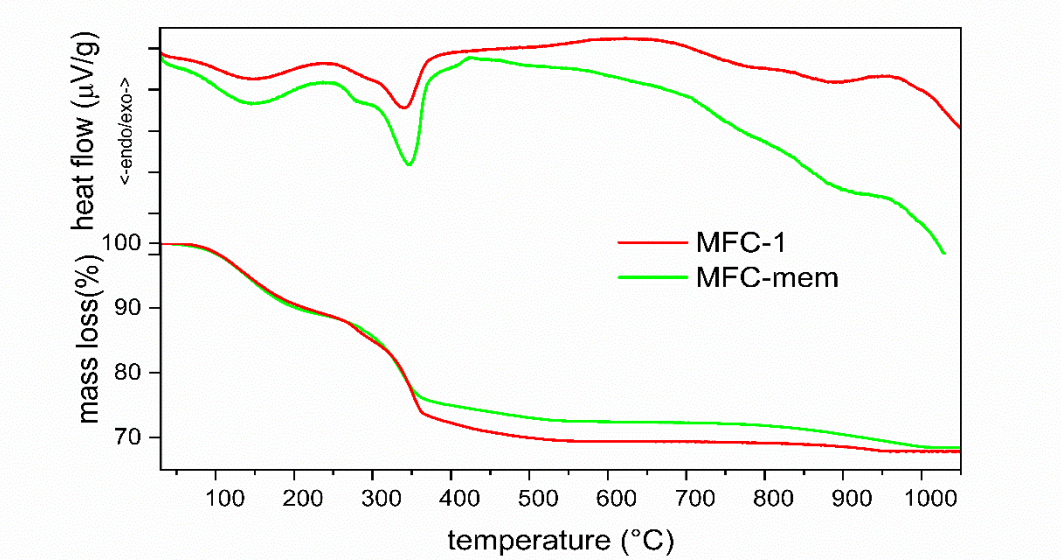

Figure 31: TG-DTA of MFC-1 (red) and MFC-mem (green)

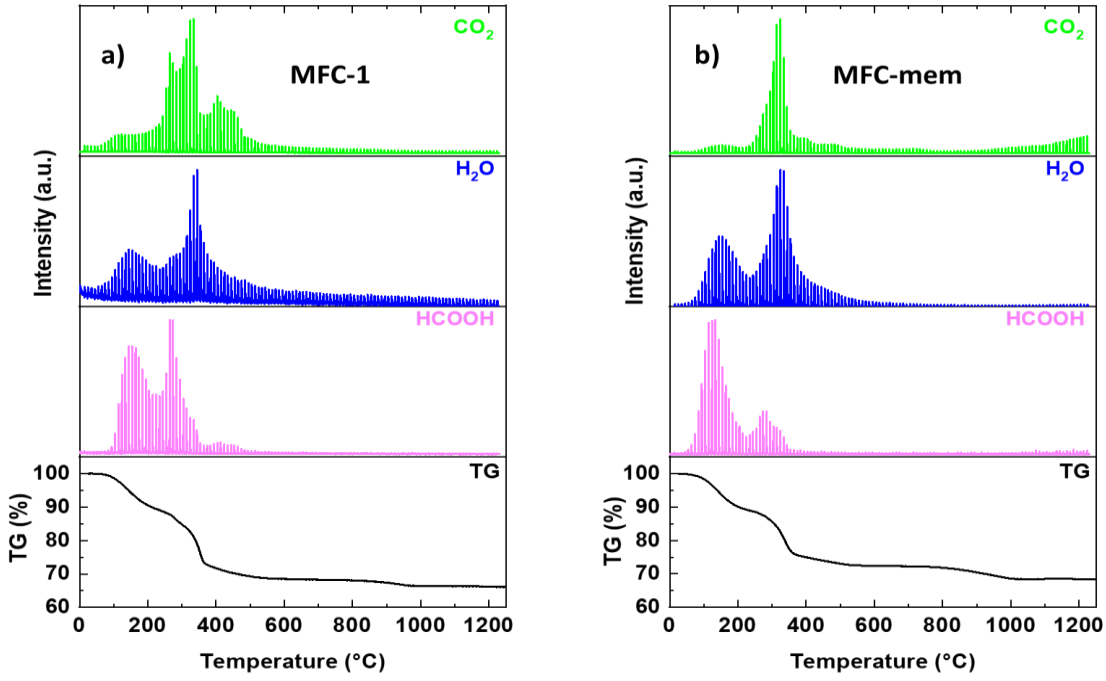

Figure 32: TG-MS trace of water, carbon dioxide and formic acid of MFC-1 a) and MFC-mem b)

2.4.2. NiAl-citrate

This material is quite different respect to the above described LDHs, it presents an organic anion at the interlayer (the citrate). Furthermore, if synthetized following the "hydrolytic polymerization" method it is constituted of homogeneously distributed hexagonal single layers.

Figure 33a illustrates the characteristic diffraction pattern observed in turbostratic LDH materials. The pattern includes "basal reflections" (00l) occurring at 2θ < 30 °, "fin-like reflections" (0kl) and (h0l) between 30 ° and 55 °, and the emergence of (110) reflections after 60 ° *(91–93)*. The calculated lattice parameters are determined as a = 0.3019 nm and c = 3.669 nm. The value of $d_{(003)}$ serves as an indicator for the space occupied by a NiAl octahedron and the interlayer region (basal spacing) *(73)*. For NiAl-citrate, the calculated $d_{(003)}$ value is approximately 1.223 nm, while the interlayer dimension, as proposed by Conterosito et al. *(74)*, is determined to be 0.743 nm.

In the TEM image of the compound (fig. 33b), a nearly single-layer plate structure is evident. Each plate measures approximately 200 nm in width and 1/2 nm in height, consistent with the findings of Piccinni et al. *(60)*.

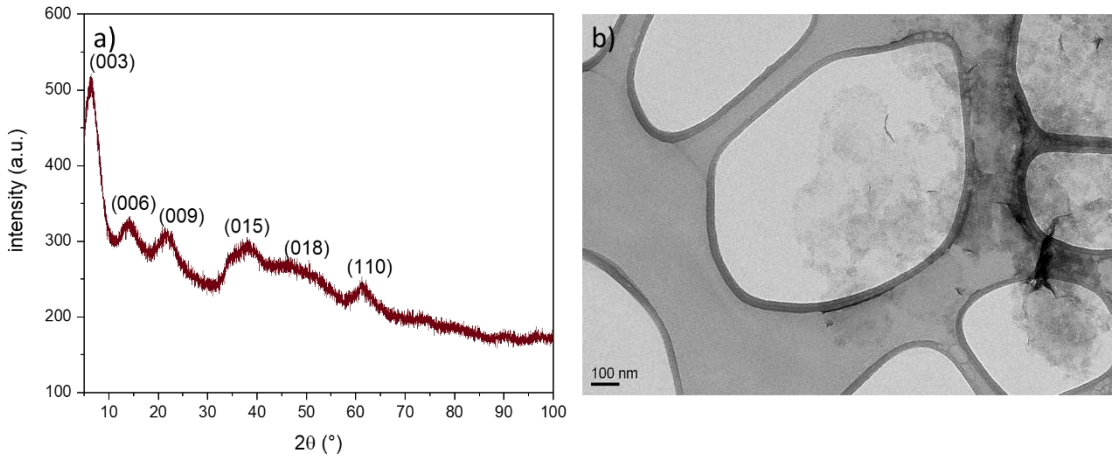

Figure 33: PXRD pattern a) and TEM image b) of NiAl-citrate LDH

Due to those characteristics the material seems to be a promising candidate for different purposes, mainly as the capture of pollutants and as catalyst precursor, to confirm these hypotheses where performed some preliminary experiments on both those directions.

The citrate is well known to be able to chelate several metals such as the toxic Pb^{2+} *(94,95)*. So, being a solid material functionalised with citrate, this LDH could be a very interesting candidate for its blocking.

A preliminary test was done, the lead concentration was analysed before and after the treatment by means of ICP-OES and the data reported in table 3 demonstrate an almost complete elimination of the pollutant.

Is worthy of mention also underline that in contrast with classic LDH, NiAl-citrate can capture cations instead of anions. This characteristic is quite unusual and could lead to

verry interesting applications as the synergic capture of both anionic and cationic pollutants.

Table 3: Pb concentration in the initial solution and after the treatment with NiAl-citrate

	Pb (ppm)	Instrumental standard deviation (ppm)
Before treatment	137.3	3.3
After treatment 1	1.47	0.57
After treatment 2	1.53	0.54

It was also decided to investigate the behaviour of the material upon heating, in fact the presence of an organic molecule at the interlayer could lead to the formation of different compounds varying the environment of reaction.

The TG-DTA curve in air (figure 34) exhibits an initial mass loss of 13 % between 30 °C and 150 °C, accompanied by a broad endothermic peak. This phenomenon is attributed to the removal of structural water. As the temperature increases, various exothermic processes occur, associated with the combustion of citrate and the conversion of LDH into oxide, resulting in a total mass loss of 39 %. After thermal treatment, the material results into a green fine powder. PXRD analysis (figure 35a) reveals well-defined diffraction peaks corresponding to cubic NiO and spinel-like Al_2NiO_4, consistent with literature findings for other LDHs *(59,96)*.

Based on these outcomes and X-ray fluorescence (XRF) data (appendix 4.5.), it is feasible to determine the precise amount of crystal water in the LDH formula (Eq. 20):

$$\left[Al_{0,14}Ni_{0,86}(OH)_2\right](NaC_6H_5O_7)_{0,07} \cdot H_2O \qquad (eq.\,20)$$

As the TGA under an inert atmosphere (Ar) (Figure 33), the initial 13 % mass loss is associated with a broad endothermic peak, attributed to LDH dehydration.

Continuing the heating process results in two significant mass losses. The first, occurring between 320 °C and 430 °C, leads to a 38 % mass loss with an endothermic peak. This is attributed to the conversion of LDH into oxide and certain rearrangements of the citrate anion. The second mass loss, from 430 °C to 530 °C, results in a total mass loss of 55 % and is connected to an endothermic peak linked to the pyrolysis of citrate, generating CO and subsequent reduction of metal oxides.

PXRD analysis of the materials post-TGA (figure 35b) reveals a predominant phase identified as metallic Ni, along with two minor phases attributable to NiO and Al_2NiO_4.

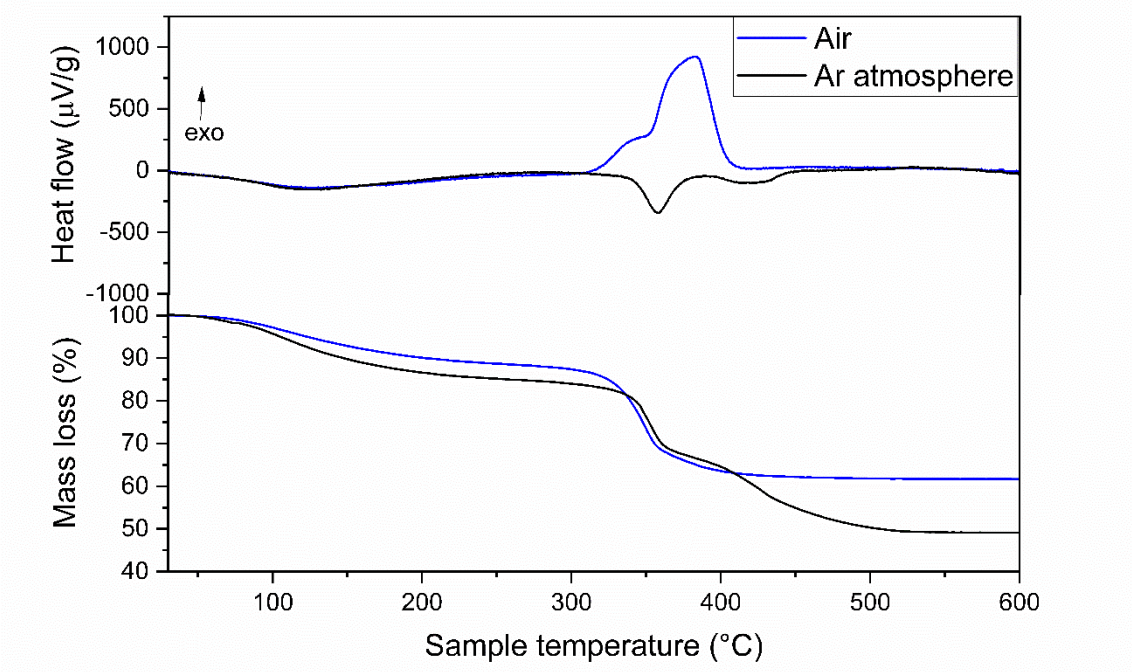

Figure 34: TG-DTA curves of NiAl-citrate in air (blue) and Ar atmosphere (black)

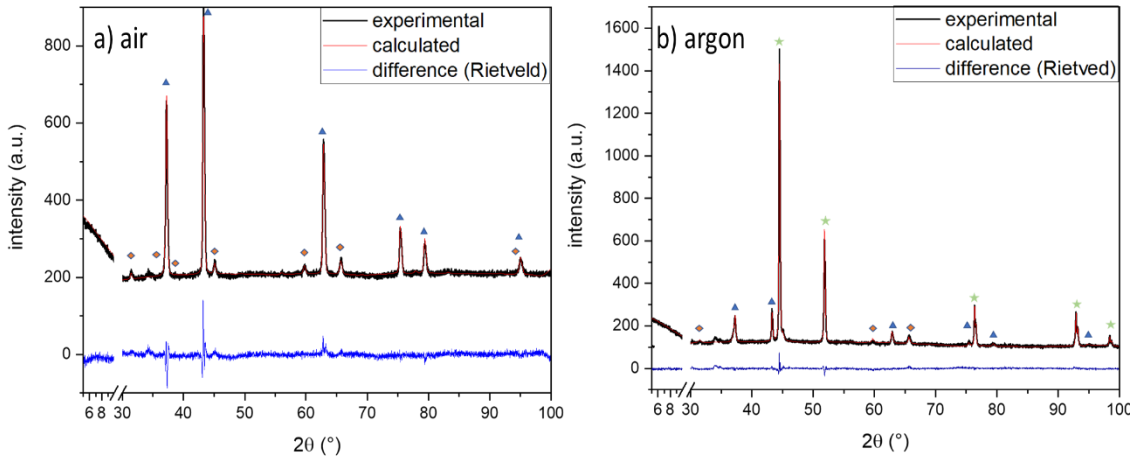

Figure 35: PXRD pattern of NiAl-citrate after the thermal treatment in dry air a) and Ar atmosphere b). Where blue triangles) are attributable to NiO, orange rhombus Al_2NiO_4 and green stars metallic Ni

To confirm the hypothesized reactivity under heating, the TG analysis was replicated in an argon (Ar) atmosphere. The experimental conditions were identical, with the heating process halted at the conclusion of each observed mass loss. Subsequently, the samples underwent a rapid cooling process (30 °C/min). The resulting compounds were then subjected to characterization through PXRD.

As depicted in Figure 36, the material calcined at 320 °C, immediately after the initial endothermal reaction, exhibits an amorphous that closely resembles the pristine Layered Double Hydroxide (LDH), resulting from dehydration and subsequent distortion of the original arrangement. After the second step, the material appears to be a blend of low-crystalline cubic structure oxides, primarily NiO. However, at 530 °C, the predominant diffraction peak at 43 ° vanishes, replaced by two new signals at 44.5 ° and 55.5 °, attributed to metallic Ni. Nickel oxide persists, as evidenced by the peak at 39 ° and the left shoulder of the primary peak.

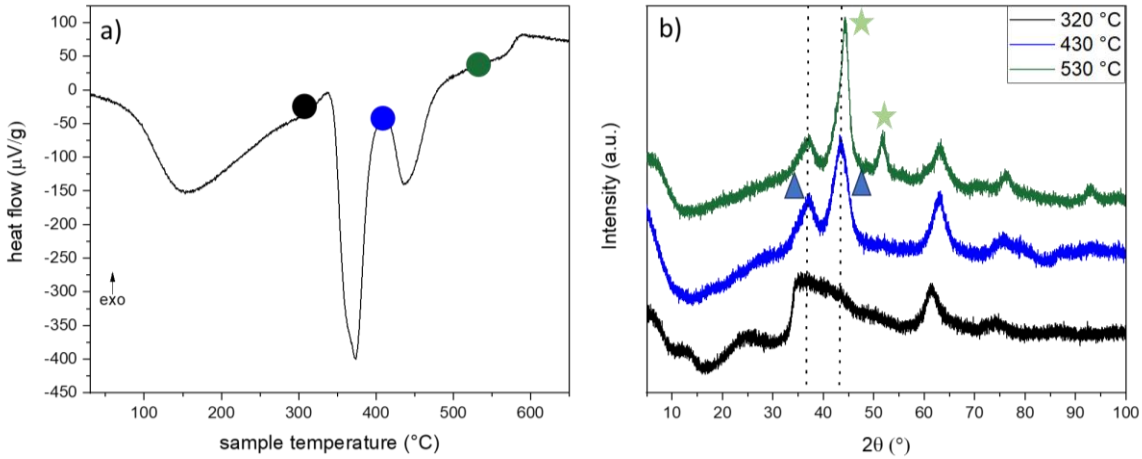

Figure 36: DTA curve of NiAl-citrate in Ar atmosphere a) where the colored circles represent the temperature at which were recorded the PXRD presented in b). blue triangles represent NiO and green stars metallic Ni

Based on the characterization findings, was prepared a sample of NiAl-cit pyrolyzed at 530 °C.

The Field Emission Scanning Electron Microscopy (FE-SEM) image (fig. 37a) reveals nanopatterning in the pyrolyzed material, showcasing non-uniform dimensions and shapes of particles, these are expected characteristics in the context of an explosive reaction. Despite this heterogeneity, the material predominantly consists of flakes.

Figure 37b displays the adsorption and desorption isotherms for the material, exhibiting a shape reminiscent of Type I in the IUPAC classification. The presence of a small H4

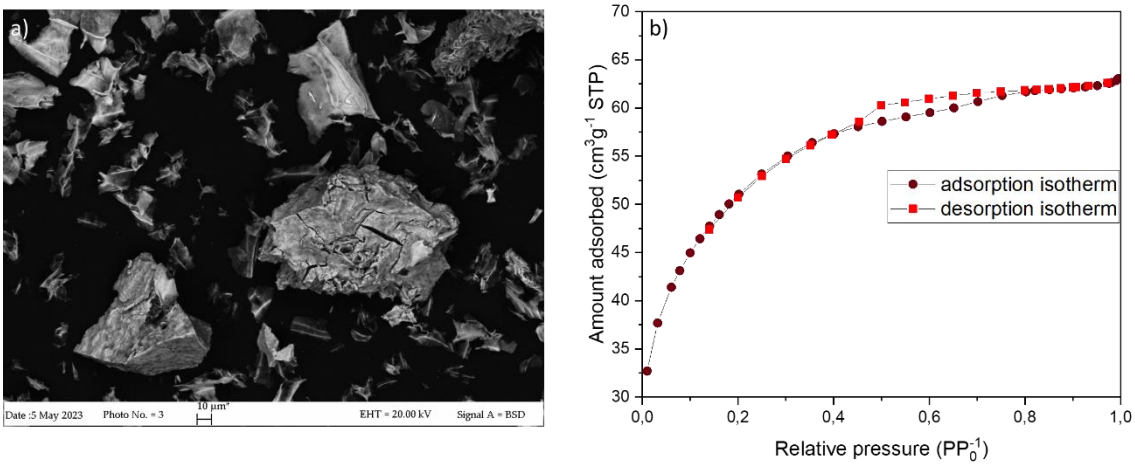

Figure 37: FE-SEM photo NiAl-pyrolyzed a) and its adsorption (dark red) and desorption (light red) isotherms at 77 K b)

hysteresis loop suggests mesoporosity (between 2 and 50 nm), shifted toward lower values *(97)*. The microporous nature of the isotherm aligns with the flake structure of the catalyst. The estimated surface area of the material, calculated using the BET model, yields a value of 177 m^2/g.

This value is very high and could be reasonably compared with some Ni based catalysts; it outclasses the Ni doped CeO_2 obtained by wet impregnation technique (~ 80/100 m^2g^{-1}) and is like $NiAl_2O_4$ produced through combustion synthesis (~ 180 m^2g^{-1}) *(98,99)*.

For this reason, was decided to test it, as catalyst in the Dry Reforming of Methane (DRM) reaction in collaboration with the research group "membrane&membrane", DCCI, UNIGE.

DRM presents an intriguing process wherein greenhouse gases, namely CO_2 and CH_4, can be transformed into syngas, a mixture of H_2 and CO with diverse applications in energy production, the synthesis of crucial chemical products, and liquid fuels *(100,101)* However, its application in industrial-scale processes faces limitations due to the elevated temperature required to overcome the endothermic nature of the production reaction (approximately 800 °C), the considerable cost associated with the most effective noble-metal catalysts (Ir, Pt, Rh), and their rapid deactivation within the reaction environment. This deactivation primarily results from the deposition of solid carbon on the catalyst surface in the form of an amorphous layer, nanotubes, or whiskers, leading to a temporary or even permanent loss of activity *(102)*. Consequently, there is active research into the use of innovative nickel catalysts for this reaction, as their cost is significantly lower than that of noble metals.

Catalytic assessments were conducted on the pyrolyzed sample, revealing its activity in the DRM reaction. This is evidenced by the CH_4 mass % conversion, depicted in figure 31a) as a function of reaction temperature. The trend in figure 38a) shows an initial near-zero % conversion, rising steadily with temperature until reaching around 15 mass %. Throughout the temperature range, experimental values consistently remain below equilibrium, with a decline in curve steepness at higher temperatures. The calculated yield of hydrogen, a key product, is presented in figure 38b). Hydrogen demonstrates a rapid increase with temperature but stays below the equilibrium conversion across the entire investigated temperature range.

Given the process's primary goal of syngas production, an assessment of the H_2/CO ratio in the obtained gas has been conducted. Figure 38c provides insights into product quality and process selectivity. The values, consistently below unity (the maximum theoretical value based on DRM stoichiometry) and below calculated equilibrium values, suggest the occurrence of secondary reactions. These reactions contribute to a decrease in the H_2/CO ratio. However, the catalyst exhibits an inclination to enhance selectivity towards hydrogen at higher temperatures. The reverse water gas shift reaction likely influences the H_2/CO ratio at lower temperatures, while the catalyst's poor activity towards methane decomposition, an endothermic reaction leading to carbon deposition, may contribute to this effect.

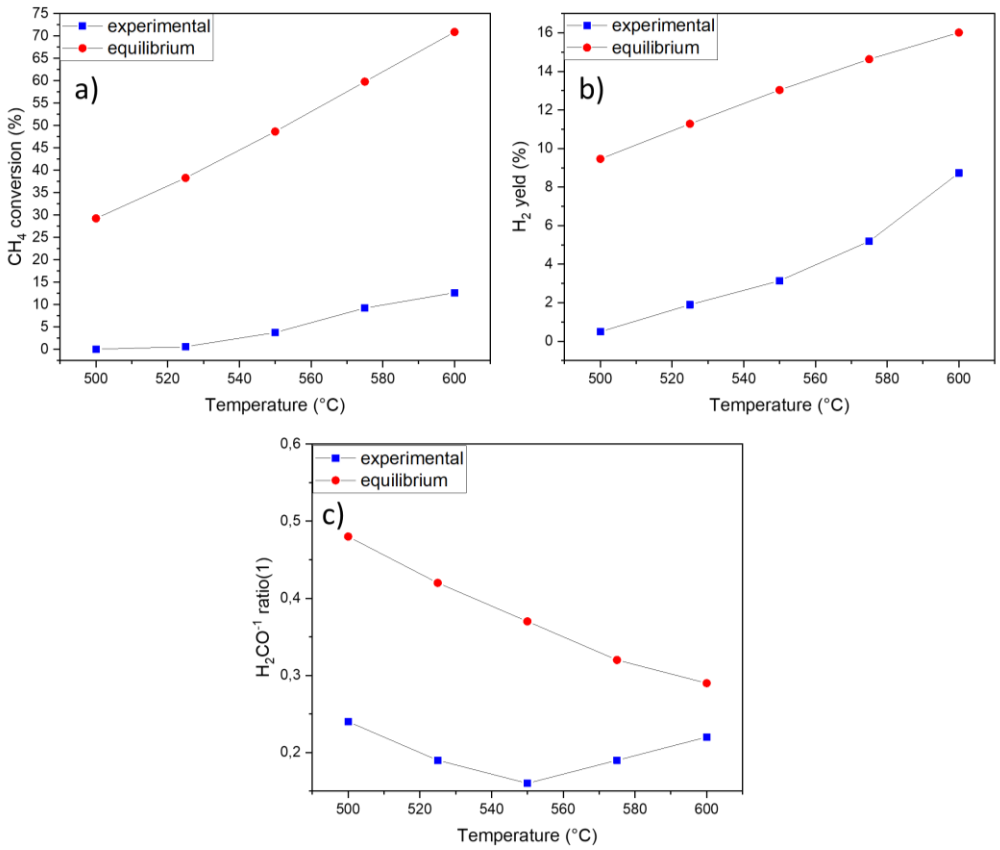

Figure 38: CH_4 % conversion values as a function of reaction temperature a); H_2 % yield as a function of reaction temperature b); H_2/CO ratio in the product stream as function of reaction temperature c). in blue are displayed experimental values and in red the calculated equilibrium ones.

3. Conclusions

In this work was investigated the applicability of LDHs as active anodic materials in rechargeable metal ion batteries, in particular LIBs and SIBs. Being a pioneering work and not having almost any literature, especially for what concern sodium-based devices, it was followed a "trial and error" approach. different compounds were synthesized and preliminary tested, only two (NiAl-NO_3 and NiFe-NO_3) have showed good performances so that they have been deeper investigated; on the other hand, some of the not selected but completely characterized LDH were chosen for other applications.

All the LDHs present an extremely high initial capacity, both in LIBs (~ 2000 mAh/g) and SIBs (~ 1000 mAh/g), followed by a marked ICL leading to only a 50 % retention after the first cycle, this behavior is quite predictable and is typical of conversion materials as part of the electrolyte is consumed to "activate" the material and form the SEI. The continuous capacity loss in the following cycles rather than the stabilization is not predictable *a priori but* is connected to the composition of the LDH and the formation of stable species.

For what concern the application in LIBs in this work was investigated NiFe-NO_3. Through a combined study involving thermal analysis and electrochemical tests, was demonstrated the influence of the LDH structure in the electrochemical performances, suggesting the occurrence of some reversible reactions, at 1.6 V in discharge and 1.1V in recharge, that gradually disappear with the loosing of dimensionality of the material.

The pristine material (NiFe-NO_3) shows a very high initial capacity (2200 mAh/g), but it undergoes a marked ICL retaining only the 30 % of it in the second cycle; after that the material stabilizes in few charge/discharge processes and after 50 cycles still deliver more than 500 mAh/g. This value is lower but still comparable with the NiO based electrodes for LIBs (between 400 and 1000 mAh/g)*(72)* but if is taken in account the amount of Ni mass % in the two compounds the ranking is overturned. In fact, NiFe-NO_3 LDH presents only a 22 mass % of Ni, while in NiO the Ni content is ~ 80 mass %. Nichel is a critical raw material and lowering its amount, without compromising too much the electrode performances, is one of the goals to achieve more sustainable and economical batteries.

Conversely in SIBs was demonstrated that two similar compounds, NiFe-NO_3 and NiAl-NO_3, behave in a completely different way. At the start both the materials deliver more than 1000 mAh/g, but after the two GCPL the pathways diverge: NIAl-NO_3 continues to lose capacity arriving around 100 mAh/g in circa 10 cycles, while NiFe-NO_3 in few cycles stabilize around 500 mAh/g. This trend could be justified by the presence in the CV plot of different peaks related also to the reduction of Fe and the XPS analysis that states that Ni (II) is never reduced to Ni(0), in fact is known in literature that the direct oxygen bond Ni-O-Fe stabilizes the oxidation state of Ni at the expense of Fe*(83)*. With this mechanism there are no complete conversion reactions that lead to the formation of metallic Ni with a dramatic volume change and the integrity of the electrode is preserved.

Another component contributing to the stability of the material seems to be NO_3^-, starting from the same matrix, NiFe LDH, and substituting the NO_3^- with the CrO_4^{2-} with a simple ion exchange mechanism, the stability immediately drops. In the CV plot the peaks related to the redox reaction Ni^{2+}/Ni^0 (0.7 V in reduction and 2 V in oxidation) suddenly reappear and the material continues to lose capacity while cycling.

The precise reactivity of the nitrate still has to be demonstrated but seems to play a key role in the stabilization of the SEI and the integrity of the electrode. Furthermore, the theoretical specific capacity of NiFe-NO_3, considering only Ni and Fe as redox centers, in SIBs is 477 mAh/g, while the experimental data are higher even after 50 cycles, demonstrating that some other reversible reactions happen.

Until now the most likely mechanism of reaction is the one expressed in equation 15:

$$\mathrm{NiFe-NO_3\ LDH} \rightarrow \mathrm{Fe_3O_4};\ \mathrm{Na_xNiO} \rightleftarrows \mathrm{NiO};\ \alpha-\mathrm{Fe_2O_3} \qquad (\mathrm{eq.}\,15)$$

In which, after the first sodiation, the material is a mixture of NiO intercalated with Na and Fe_3O_4, then it transforms in a mixture of NiO and α-Fe_2O_3 in a reversible way through a mixed intercalation/conversion mechanism, These results are very promising and could inspire further works to enlighten the role of the NO_3^- and find a way to reduce the initial ICL, making the material more competitive and appliable also in large scale for commercial uses.

Other two LDH (MgFe-Cl and NiFe-citrate) are worthy of mention, as they have found application for other tasks. By serendipity it was discovered that MgFe-LDH could catalyze the formation of formic acid staring from water and carbon dioxide as expressed in equation 19.

$$2\mathrm{CO_2} + 2\mathrm{H_2O} \xrightarrow{\Delta\mathrm{T-LDH}} 2\mathrm{HCOOH} + \mathrm{O_2} \qquad (eq.\,19)$$

This mechanism still needs a deeper study since the main goal of the work was to synthesize a pure MgFe-Cl LDH and this compound was discovered by chance.

As concerns the NiAl-citrate, the simple synthesis of the material throw "hydrolytic polymerization" is just a result. In fact, the method is quite new, and, in the literature, it has been applied only for the synthesis of NiFe-citrate, having been able to synthesize a different LDH has demonstrated the stability and replicability of the synthetic path *(60)*. The material seems to be a promising candidate for the absorption of heavy metals ions (as Pb^{2+}) exploiting the property of chelation of the citrate but could also work as an anion exchanger (as other LDH) making it very interesting for some experiments of simultaneous absorption.

The presence of the interlayered citrate makes the material very interesting also for catalysis, its pyrolysis leads to the formation of a nanopatterned compound almost entirely made up of Ni^0. Physisorption measurements indicate that the pyrolyzed NiAl-citrate possesses a notably large BET specific surface area, approximately 177 m^2g^{-1}, and exhibits a distinctive type I isotherm. This isotherm pattern is linked to the observed flake structure confirmed by electron microscopy. The specific surface area achieved through

this method is higher or like the one obtained through similar synthetic paths, as wet impregnation, and is comparable to the one achieved through more complex and expensive routes such as the combustion method.

Furthermore, the material demonstrated activity in preliminary tests for the Dry Reforming of Methane (DRM) reaction. The tests revealed an increase in hydrogen (H_2) yield with rising temperature. Surprisingly, the H_2/CO ratio was lower than anticipated for the DRM reaction alone, suggesting the occurrence of additional reactions such as the reverse water gas shift reaction. these secondary reactions became less significant with increasing temperature, as evidenced by the rising H_2/CO ratio.

It is hoped that all the work presented in this thesis will stimulate the curiosity of other researchers about the Layered Double Hydroxides and their potential applications and help the production of new and more sustainable batteries to overcome the challenges of the future.

4. Appendix

4.1. Amounts of products determination in activity tests

The concentration percentage of product i, denoted as Ci %, was determined using the response factor of TCD (eq. A1)

$$\mathrm{Ci\%} = \frac{\mathrm{Area_i}}{\mathrm{F_{r_i}}} \qquad (eq.\mathrm{A1})$$

Here, $\mathrm{Area_i}$ represents the chromatographic area of product i, and F_{r_I} denotes the instrument response factor specific to each gas. The molar chromatographic flow, CMP, was determined using equation A2.

$$\mathrm{CMPi}\ \left[\frac{\mathrm{mol}}{\mathrm{min}}\right] = \frac{\mathrm{Q_{vol\ in}} \cdot \left(\frac{\mathrm{Ci\%}}{100}\right)}{\frac{1000}{\mathrm{RT}}} \qquad (\mathrm{eq.A2})$$

Here, $Q_{vol\ in}$ represents the volumetric flow entering the reactor $[\frac{mL}{min}]$, C % is the percentage concentration, R is the universal gas constant $[\frac{L \cdot atm}{mol \cdot K}]$, and T is the absolute temperature [K].

The provided values enable the computation of methane (CH_4) and carbon dioxide (CO_2) percentage conversion (equations A3 and A4), hydrogen (H_2) percentage yield (equation A5), and the H_2/CO ratio (equation A7).

$$CH_4\%\ conversion = \frac{\left(CMP_{CH_4 in} - CMP_{CH_4 out}\right) \cdot 100}{CMP_{CH_4 in}} \qquad (eq.A3)$$

$$CO_2\%\ conversion = \frac{\left(CMP_{CO_2 in} - CMP_{CO_2 out}\right) \cdot 100}{CMP_{CO_2 in}} \qquad (eq.A4)$$

$$H_2\%\ Yield = \frac{CMP_{H_2\ out}}{CMP_{H_2\ theoric\ out}} \cdot 100 = \frac{CMP_{H_2\ out}}{2CMP_{CH_4\ in}} \cdot 100 \qquad (eq.A5)$$

$$\frac{H_2}{CO} = \frac{CMP_{H_2}}{CMP_{CO}} \qquad (eq.A6)$$

Equilibrium values were determined using software designed for minimizing Gibbs energy. For this study, a simplified reaction environment consisting solely of the primary species in the gas phase was considered: CO_2, CO, CH_4, H_2, H_2O, N_2.

4.2. Trasatti Method

It is a method that could gave information on the nature of the processes that happen in an electrochemical reaction. It is based on Cottrell equation (eq.A7) that assumes that the total capacity (q_{tot}) is a sum of the inner (q_i) and outer (q_o) contribution (diffusion and capacitance) (eq.A8).

$$q(v) \propto \sqrt{V} \qquad (\text{eq. A7})$$

$$q_{tot} = q_i + q_o \qquad (\text{eq. A8})$$

In a CV if the scan rate is very high only the outer processes could occur, there is no time available for diffusion, vice versa if the scan rate is very low all the possible diffusion processes must be taken in consideration obtaining the eq.s. A9 and A10 that allow the graphical extrapolation of q_o and q_{tot}.

$$v \to \infty \Rightarrow q \to q_o \qquad q_{(v)} = \frac{k}{\sqrt{v}} + q_o \qquad (\text{eq. A9})$$

$$v \to 0 \Rightarrow q \to q_{tot} \qquad \frac{1}{q_{(v)}} = k\sqrt{v} + \frac{1}{q_{tot}} \qquad (\text{eq. A10})$$

4.3. Other magnetic studies on NiFe-NO_3

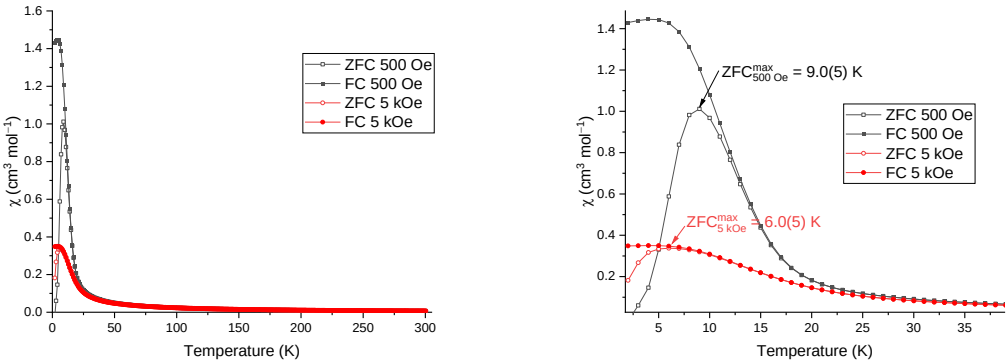

Figure A1: ZFC/FC susceptibilities obtained for 500 Oe and 5 kOe for pristine NiFe-LDH powder.

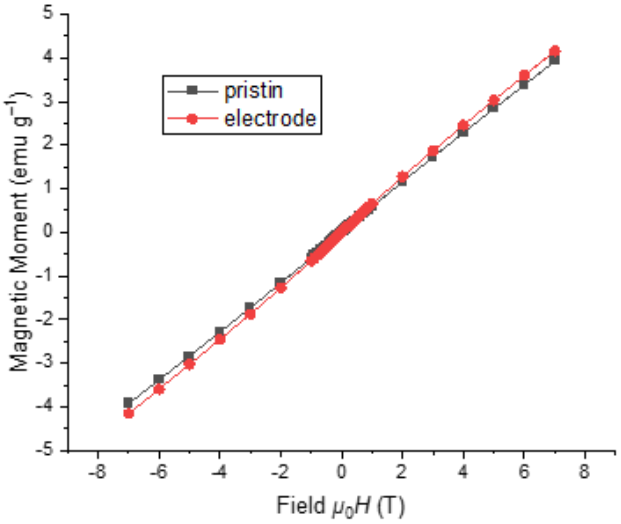

Figure A2: Magnetic moment vs. field scan obtained at 300 K for NiFe-LDH pristine powder and for the pristine electrode material where only the mass of the active NiFe-LDH has been considered.

4.4. NiFe-CrO_4 characterization

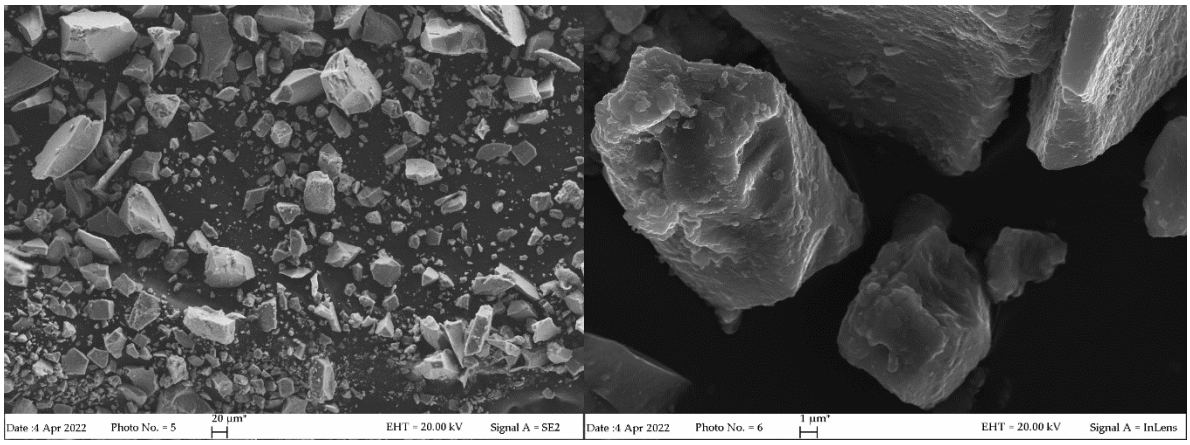

Figure A3: FE-SEM at low and high magnification of NiFe-CrO_4

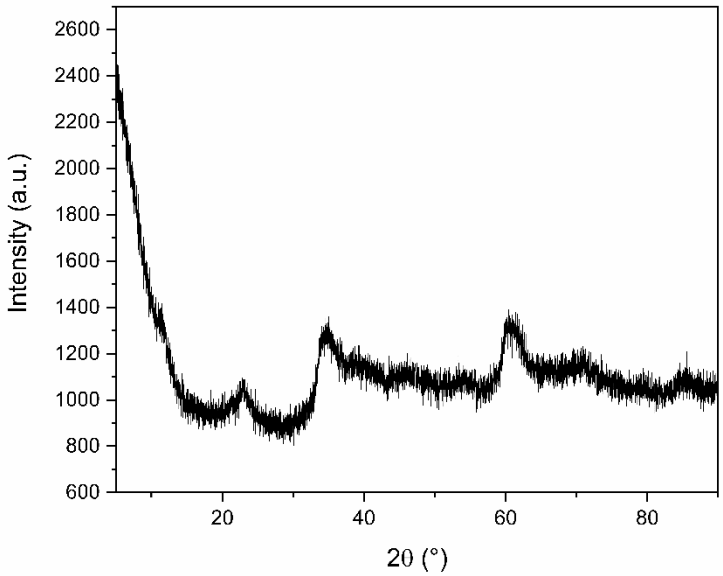

Figure A4: PXRD pattern of NiFe-CrO_4

4.5 XRF data of NiAl-citrate

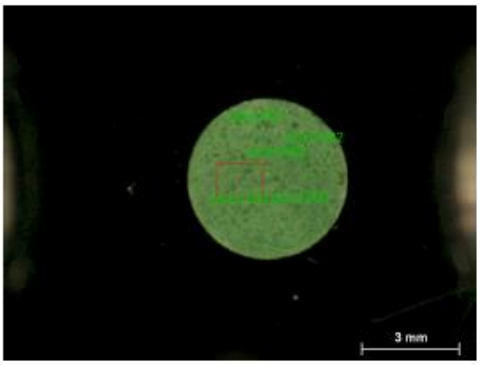

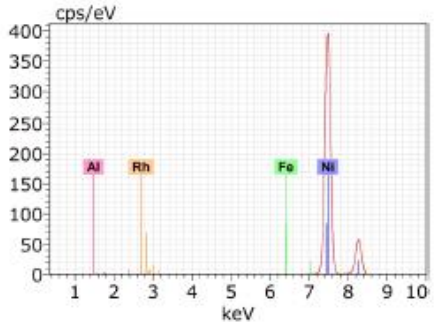

Point 1

Spectrum:

El	AN	Series	Net	unn. C [wt.%]	norm. C [wt.%]	Atom. C [at.%]	Error (1 Sigma) [wt.%]
Al	13	K-series	9595	5.71	7.35	14.72	0.06
Fe	26	K-series	11716	0.05	0.06	0.06	0.00
Ni	28	K-series	9225552	71.87	92.59	85.22	0.02
Rh	45	K-series	11230	0.00	0.00	0.00	0.00
Total:				77.63	100.00	100.00	

Point 2

Spectrum:

El	AN	Series	Net	unn. C [wt.%]	norm. C [wt.%]	Atom. C [at.%]	Error (1 Sigma) [wt.%]
Al	13	K-series	7180	5.32	6.85	13.78	0.06
Fe	26	K-series	8459	0.04	0.06	0.05	0.00
Ni	28	K-series	7448877	72.32	93.10	86.16	0.03
Rh	45	K-series	8410	0.00	0.00	0.00	0.00
Total:				77.68	100.00	100.00	

Point 3

Spectrum:

El	AN	Series	Net	unn. C [wt.%]	norm. C [wt.%]	Atom. C [at.%]	Error (1 Sigma) [wt.%]
Al	13	K-series	9192	5.45	7.02	14.11	0.06
Fe	26	K-series	15945	0.06	0.08	0.08	0.00
Ni	28	K-series	9281093	72.10	92.90	85.81	0.02
Rh	45	K-series	10732	0.00	0.00	0.00	0.00
Total:				77.61	100.00	100.00	

Point 4

Spectrum:

El	AN	Series	Net	unn. C [wt.%]	norm. C [wt.%]	Atom. C [at.%]	Error (1 Sigma) [wt.%]
Al	13	K-series	9285	5.51	7.10	14.25	0.06
Fe	26	K-series	17870	0.07	0.09	0.09	0.00
Ni	28	K-series	9268172	72.07	92.81	85.66	0.02
Rh	45	K-series	10784	0.00	0.00	0.00	0.00
Total:				77.65	100.00	100.00	

Point 5

Spectrum:

El	AN	Series	Net	unn. C [wt.%]	norm. C [wt.%]	Atom. C [at.%]	Error (1 Sigma) [wt.%]
Al	13	K-series	4578	5.49	7.09	14.23	0.08
Fe	26	K-series	6221	0.05	0.07	0.06	0.00
Ni	28	K-series	4577818	71.88	92.85	85.71	0.03
Rh	45	K-series	5450	0.00	0.00	0.00	0.00
Total:				77.42	100.00	100.00	

Figure A5: XRF analysis on different points of a NIAl-citrate samples, the values in the square are the atomic percentage of each species.

5. Bibliography

1. *Our World in Data*. https://ourworldindata.org/.

2. Goodenough, J. B.; Park, K.-S. The Li-Ion Rechargeable Battery: A Perspective. *Journal of the American Chemical Society* **2013**, *135*(4), 1167–1176. doi:10.1021/ja3091438.

3. Nitta, N.; Wu, F.; Lee, J. T.; Yushin, G. Li-ion battery materials: present and future. *Materials Today* **2015**, *18*(5), 252–264. doi:https://doi.org/10.1016/j.mattod.2014.10.040.

4. Hwang, J. Y.; Myung, S. T.; Sun, Y. K. Sodium-ion batteries: Present and future. *Chemical Society Reviews*. Royal Society of Chemistry June 21, 2017, pp 3529–3614. doi:10.1039/c6cs00776g.

5. Slater, M. D.; Kim, D.; Lee, E.; Johnson, C. S. Sodium-ion batteries. *Advanced Functional Materials* **2013**, *23*(8), 947–958. doi:10.1002/adfm.201200691.

6. Kundu, D.; Talaie, E.; Duffort, V.; Nazar, L. F. The emerging chemistry of sodium ion batteries for electrochemical energy storage. *Angewandte Chemie - International Edition* **2015**, *54*(11), 3432–3448. doi:10.1002/anie.201410376.

7. Liu, C.; Li, F.; Ma, L.-P.; Cheng, H.-M. Advanced Materials for Energy Storage. *Advanced Materials* **2010**, *22*(8), E28–E62. doi:doi:10.1002/adma.200903328.

8. Liu, Y.; Wang, Y. M.; Yakobson, B. I.; Wood, B. C. Assessing Carbon-Based Anodes for Lithium-Ion Batteries: A Universal Description of Charge-Transfer Binding. *Phys. Rev. Lett.* **2014**, *113*(2), 28304. doi:10.1103/PhysRevLett.113.028304.

9. Raccichini, R.; Varzi, A.; Passerini, S.; Scrosati, B. The role of graphene for electrochemical energy storage. *Nature Materials* **2015**, *14*(3), 271–279. doi:10.1038/nmat4170.

10. Xie, L.; Tang, C.; Bi, Z.; Song, M.; Fan, Y.; Yan, C.; et al. Hard Carbon Anodes for Next-Generation Li-Ion Batteries: Review and Perspective. *Advanced Energy Materials* **2021**, *11*(38), 2101650. doi:https://doi.org/10.1002/aenm.202101650.

11. Yang, Z.; Choi, D.; Kerisit, S.; Rosso, K. M.; Wang, D.; Zhang, J.; et al. Nanostructures and lithium electrochemical reactivity of lithium titanites and titanium oxides: A review. *Journal of Power Sources* **2009**, *192*(2), 588–598. doi:10.1016/j.jpowsour.2009.02.038.

12. Ge, P.; Fouletier, M. Electrochemical intercalation of sodium in graphite. *Solid State Ionics* **1988**, *28–30*, 1172–1175. doi:10.1016/0167-2738(88)90351-7.

13. Shao, W.; Shi, H.; Jian, X.; Wu, Z.-S.; Hu, F. Hard-Carbon Anodes for Sodium-Ion Batteries: Recent Status and Challenging Perspectives. *Advanced Energy and Sustainability Research* **2022**, *3*(7), 2200009. doi:https://doi.org/10.1002/aesr.202200009.

14. Liu, Z.-G.; Du, R.; He, X.-X.; Wang, J.-C.; Qiao, Y.; Li, L.; et al. Recent Progress on Intercalation-Based Anode Materials for Low-Cost Sodium-Ion Batteries. *ChemSusChem* **2021**, *14*(18), 3724–3743. doi:https://doi.org/10.1002/cssc.202101186.

15. Cabana, J.; Monconduit, L.; Larcher, D.; Palacín, M. R. Beyond Intercalation-Based Li-Ion Batteries: The State of the Art and Challenges of Electrode Materials Reacting Through Conversion Reactions. *Advanced Materials* **2010**, *22*(35), E170–E192. doi:doi:10.1002/adma.201000717.

16. Kraytsberg, A.; Ein-Eli, Y. A critical review-promises and barriers of conversion electrodes for Li-ion batteries. *Journal of Solid State Electrochemistry* **2017**, *21*(7), 1907–1923. doi:10.1007/s10008-017-3580-9.

17. Wu, C.; Dou, S.-X.; Yu, Y. The State and Challenges of Anode Materials Based on Conversion Reactions for Sodium Storage. *Small* **2018**, *14*(22), 1703671. doi:https://doi.org/10.1002/smll.201703671.

18. Su, X.; Wu, Q.; Li, J.; Xiao, X.; Lott, A.; Lu, W.; et al. Silicon-Based Nanomaterials for Lithium-Ion Batteries: A Review. *Advanced Energy Materials* **2014**, *4*(1), 1300882. doi:doi:10.1002/aenm.201300882.

19. Wang, B.; Luo, B.; Li, X.; Zhi, L. The dimensionality of Sn anodes in Li-ion batteries. *Materials Today* **2012**, *15*(12), 544–552. doi:https://doi.org/10.1016/S1369-7021(13)70012-9.

20. Komaba, S.; Matsuura, Y.; Ishikawa, T.; Yabuuchi, N.; Murata, W.; Kuze, S. Redox reaction of Sn-polyacrylate electrodes in aprotic Na cell. *Electrochemistry Communications* **2012**, *21*, 65–68. doi:10.1016/J.ELECOM.2012.05.017.

21. Sarkar, S.; Peter, S. C. An overview on Sb-based intermetallics and alloys for sodium-ion batteries: trends, challenges and future prospects from material synthesis to battery performance. *J. Mater. Chem. A* **2021**, *9*(9), 5164–5196. doi:10.1039/D0TA12063D.

22. Liu, W.; Zhi, H.; Yu, X. Recent progress in phosphorus based anode materials for lithium/sodium ion batteries. *Energy Storage Materials* **2019**, *16*, 290–322. doi:10.1016/J.ENSM.2018.05.020.

23. Li, Q.; Chen, J.; Fan, L.; Kong, X.; Lu, Y. Progress in electrolytes for rechargeable Li-based batteries and beyond. *Green Energy & Environment* **2016**, *1*(1), 18–42. doi:https://doi.org/10.1016/j.gee.2016.04.006.

24. Goodenough, J. B.; Kim, Y. Challenges for Rechargeable Li Batteries. *Chemistry of Materials* **2010**, *22*(3), 587–603. doi:10.1021/cm901452z.

25. Wang, A.; Kadam, S.; Li, H.; Shi, S.; Qi, Y. Review on modeling of the anode solid electrolyte interphase (SEI) for lithium-ion batteries. *npj Computational Materials* **2018**, *4*(1). doi:10.1038/s41524-018-0064-0.

26. Cavani, F.; Trifirò, F.; Vaccari, A. Hydrotalcite-type anionic clays: Preparation, properties and applications. *Catalysis Today* **1991**, *11*(2), 173–301. doi:10.1016/0920-5861(91)80068-K.

27. Saber, O.; Tagaya, H. New Layered Double Hydroxide, Zn–Ti LDH : Preparation and Intercalation Reactions. *Journal of inclusion phenomena and macrocyclic chemistry* **2003**, *45*(1), 107–115. doi:10.1023/A:1023078728942.

28. Qu, J.; He, X.; Wang, B.; Zhong, L.; Wan, L.; Li, X.; et al. Synthesis of Li–Al layered double hydroxides via a mechanochemical route. *Applied Clay Science* **2016**, *120*, 24–27. doi:10.1016/J.CLAY.2015.11.017.

29. Sławiński, W. A.; Sjåstad, A. O.; Fjellvåg, H. Stacking Faults and Polytypes for Layered Double Hydroxides: What Can We Learn from Simulated and Experimental X-ray Powder Diffraction Data? *Inorganic Chemistry* **2016**, *55*(24), 12881–12889. doi:10.1021/acs.inorgchem.6b02247.

30. Hochstetter, C. Untersuchung über die Zusammensetzung einiger Mineralien. *Journal für praktische Chemie* **1842**, *27*, 375–378.

31. Feitknecht, W.; Gerber, M. Zur Kenntnis der Doppelhydroxyde und basischen Doppelsalze III. Über Magnesium-Aluminiumdoppelhydroxyd. *Helvetica Chimica Acta* **1942**, *25*(1), 131–137. doi:https://doi.org/10.1002/hlca.19420250115.

32. Allmann, R.; Jepsen, H. P. Die struktur des hydrotalkits. *Neu. Jb. Mineral* **1969**, *12*, 544–551.

33. Cardinale, A. M.; Carbone, C.; Consani, S.; Fortunato, M.; Parodi, N. Layered double hydroxides for remediation of industrial wastewater from a Galvanic plant. *Crystals* **2020**, *10*(6). doi:10.3390/cryst10060443.

34. Zhang, M.; Gao, B.; Yao, Y.; Inyang, M. Phosphate removal ability of biochar/MgAl-LDH ultra-fine composites prepared by liquid-phase deposition. *Chemosphere* **2013**, *92*(8), 1042–1047. doi:10.1016/J.CHEMOSPHERE.2013.02.050.

35. Ahmed, I. M.; Gasser, M. S. Adsorption study of anionic reactive dye from aqueous solution to Mg–Fe–CO3 layered double hydroxide (LDH). *Applied Surface Science* **2012**, *259*, 650–656. doi:10.1016/J.APSUSC.2012.07.092.

36. Pavan, P. C.; Crepaldi, E. L.; Valim, J. B. Sorption of Anionic Surfactants on Layered Double Hydroxides. *Journal of Colloid and Interface Science* **2000**, *229*(2), 346–352. doi:10.1006/JCIS.2000.7031.

37. Wang, P.; Yin, L.; Wang, X.; Zhao, G.; Yu, S.; Song, G.; et al. l-cysteine intercalated layered double hydroxide for highly efficient capture of U(VI) from aqueous solutions. *Journal of Environmental Management* **2018**, *217*, 468–477. doi:10.1016/J.JENVMAN.2018.03.112.

38. Mir, Z. M.; Bastos, A.; Höche, D.; Zheludkevich, M. L. Recent Advances on the Application of Layered Double Hydroxides in Concrete—A Review. *Materials* **2020**, *13*(6). doi:10.3390/ma13061426.

39. Becker, C. M.; Gabbardo, A. D.; Wypych, F.; Amico, S. C. Mechanical and flame-retardant properties of epoxy/Mg–Al LDH composites. *Composites Part A: Applied Science and Manufacturing* **2011**, *42*(2), 196–202. doi:10.1016/J.COMPOSITESA.2010.11.005.

40. Hu, T.; Gu, Z.; Williams, G. R.; Strimaite, M.; Zha, J.; Zhou, Z.; et al. Layered double hydroxide-based nanomaterials for biomedical applications. *Chemical Society Reviews*. Royal Society of Chemistry July 6, 2022, pp 6126–6176. doi:10.1039/d2cs00236a.

41. Bejoy, N. Hydrotalcite. *Resonance* **2001**, *6*(2), 57–61. doi:10.1007/BF02836942.

42. Cardinale, A. M.; Vecchio Ciprioti, S.; Fortunato, M.; Catauro, M. Thermal behavior and antibacterial studies of a carbonate Mg–Al-based layered double hydroxide (LDH) for in vivo uses. *Journal of Thermal Analysis and Calorimetry* **2022**, *148*(4), 1523–1532. doi:10.1007/s10973-022-11334-3.

43. Cardinale, A. M.; Alberti, S.; Reverberi, A. Pietro; Catauro, M.; Ghibaudo, N.; Fortunato, M. Antibacterial and Photocatalytic Activities of LDH-Based Sorbents of Different Compositions. *Microorganisms* **2023**, *11*(4), 1045. doi:10.3390/microorganisms11041045.

44. Bodhankar, P. M.; Sarawade, P. B.; Singh, G.; Vinu, A.; Dhawale, D. S. Recent advances in highly active nanostructured NiFe LDH catalyst for electrochemical water splitting. *J. Mater. Chem. A* **2021**, *9*(6), 3180–3208. doi:10.1039/D0TA10712C.

45. Li, M.; Chen, C.; Ayvalı, T.; Suo, H.; Zheng, J.; Teixeira, I. F.; et al. CO2 Hydrogenation to Methanol over Catalysts Derived from Single Cationic Layer CuZnGa LDH Precursors. *ACS Catalysis* **2018**, *8*(5), 4390–4401. doi:10.1021/acscatal.8b00474.

46. Tanasoi, S.; Tanchoux, N.; Urdă, A.; Tichit, D.; Săndulescu, I.; Fajula, F.; et al. New Cu-based mixed oxides obtained from LDH precursors, catalysts for methane total oxidation. *Applied Catalysis A: General* **2009**, *363*(1–2), 135–142. doi:10.1016/J.APCATA.2009.05.007.

47. Wang, Y. G.; Cheng, L.; Xia, Y. Y. Electrochemical profile of nano-particle CoAl double hydroxide/active carbon supercapacitor using KOH electrolyte solution. *Journal of Power Sources* **2006**, *153*(1), 191–196. doi:10.1016/J.JPOWSOUR.2005.04.009.

48. Ray, P. K.; Mohanty, R.; Parida, K. Recent advancements of NiCo LDH and graphene based nanohybrids for supercapacitor application. *Journal of Energy Storage* **2023**, *72*, 108335. doi:10.1016/J.EST.2023.108335.

49. Zhang, R.; Xue, Z.; Qin, J.; Sawangphruk, M.; Zhang, X.; Liu, R. NiCo-LDH/Ti3C2 MXene hybrid materials for lithium ion battery with high-rate capability and long cycle life. *Journal of Energy Chemistry* **2020**, *50*, 143–153. doi:10.1016/j.jechem.2020.03.018.

50. Li, X.; Fortunato, M.; Cardinale, A. M.; Sarapulova, A.; Njel, C.; Dsoke, S. Electrochemical study on nickel aluminum layered double hydroxides as high-performance electrode material for lithium-ion batteries based on sodium alginate binder. *Journal of Solid State Electrochemistry* **2021**. doi:10.1007/s10008-021-05011-y.

51. Zhao, Y.; Sun, T.; Yin, Q.; Zhang, J.; Zhang, S.; Luo, J.; et al. Discovery of a new intercalation-type anode for high-performance sodium ion batteries. *Journal of Materials Chemistry A* **2019**, *7*(25), 15371–15377. doi:10.1039/c9ta03753e.

52. Yin, Q.; Luo, J.; Zhang, J.; Zheng, L.; Cui, G.; Han, J.; et al. High-performance, long lifetime chloride ion battery using a NiFe–Cl layered double hydroxide cathode. *J. Mater. Chem. A* **2020**, *8*(25), 12548–12555. doi:10.1039/D0TA04290K.

53. Boclair, J. W.; Braterman, P. S. Layered double hydroxide stability. 1. Relative stabilities of layered double hydroxides and their simple counterparts. *Chemistry of Materials* **1999**, *11*(2), 298–302. doi:10.1021/CM980523U.

54. He, J.; Wei, M.; Li, B.; Kang, Y.; Evans, D. G.; Duan, X. Preparation of layered double hydroxides. *Structure and Bonding* **2005**, *119*, 89–119. doi:10.1007/430_006.

55. Guo, X. L.; Liu, X. Y.; Hao, X. D.; Zhu, S. J.; Dong, F.; Wen, Z. Q.; et al. Nickel-Manganese Layered Double Hydroxide Nanosheets Supported on Nickel Foam for High-performance Supercapacitor Electrode Materials. *Electrochimica Acta* **2016**, *194*, 179–186. doi:10.1016/J.ELECTACTA.2016.02.080.

56. Rao, M. M.; Reddy, B. R.; Jayalakshmi, M.; Jaya, V. S.; Sridhar, B. Hydrothermal synthesis of Mg–Al hydrotalcites by urea hydrolysis. *Materials Research Bulletin* **2005**, *40*(2), 347–359. doi:https://doi.org/10.1016/j.materresbull.2004.10.007.

57. Mascolo, G.; Mascolo, M. C. On the synthesis of layered double hydroxides (LDHs) by reconstruction method based on the "memory effect." *Microporous and Mesoporous Materials* **2015**, *214*, 246–248. doi:10.1016/J.MICROMESO.2015.03.024.

58. Ye, H.; Liu, S.; Yu, D.; Zhou, X.; Qin, L.; Lai, C.; et al. Regeneration mechanism, modification strategy, and environment application of layered double hydroxides: Insights based on memory effect. *Coordination Chemistry Reviews* **2022**, *450*, 214253. doi:10.1016/J.CCR.2021.214253.

59. Cardinale, A. M.; Fortunato, M.; Locardi, · Federico; Parodi, N. Thermal analysis of MgFe-Cl Layered doubled hydroxide (LDH) directly synthetized and produced "via memory effect." *Journal of Thermal Analysis and Calorimetry* **2022**, *147*, 5297–5302. doi:10.1007/s10973-022-11207-9.

60. Piccinni, M.; Bellani, S.; Bianca, G.; Bonaccorso, F. Nickel–Iron Layered Double Hydroxide Dispersions in Ethanol Stabilized by Acetate Anions. *Inorganic Chemistry* **2022**, *61*(11), 4598–4608. doi:10.1021/acs.inorgchem.1c03485.

61. Still, E. R.; Wikberg, P. Solution studies of systems with polynuclear complex formation. 2. The nickel(II) citrate system. *Inorganica Chimica Acta* **1980**, *46*(C), 153–155. doi:10.1016/S0020-1693(00)84184-5.

62. Zhou, X.-W.; Du, J.-J.; Xiao, S.-Z.; Ye, D.; Dong, W.-W.; An, D.; et al. Solid and solution study of tetranuclear zinc citrates with N-donor chelates. *Journal of Coordination Chemistry* **2014**, *67*(14), 2470–2478. doi:10.1080/00958972.2014.944174.

63. Grégoire, B.; Ruby, C.; Carteret, C. Hydrolysis of mixed Ni^{2+}–Fe^{3+} and Mg^{2+}–Fe^{3+} solutions and mechanism of formation of layered double hydroxides. *Journal of the Chemical Society. Dalton Transactions* **2013**, *42*(44), 15687–15698. doi:10.1039/c3dt51521d.

64. Wu, J.; Lin, J.; Zhan, Y. Interception of phosphorus release from sediments using Mg/Fe-based layered double hydroxide (MF-LDH) and MF-LDH coated magnetite as geo-engineering tools. *Science of the Total Environment* **2020**, *739*, 139749. doi:10.1016/j.scitotenv.2020.139749.

65. Roisnel, T.; Rodríquez-Carvajal, J. WinPLOTR: A Windows Tool for Powder Diffraction Pattern Analysis. *Materials Science Forum* **2001**, *378–381*, 118–123. doi:10.4028/www.scientific.net/MSF.378-381.118.

66. Bradford, M. C. J.; Vannice, M. A. CO2 Reforming of CH4. *Catalysis Reviews* **1999**, *41*(1), 1–42. doi:10.1081/CR-100101948.

67. Bodhankar, P. M.; Sarawade, P. B.; Singh, G.; Vinu, A.; Dhawale, D. S. Recent advances in highly active nanostructured NiFe LDH catalyst for electrochemical water splitting. **2020**. doi:10.1039/d0ta10712c.

68. Zhou, H.; Wu, F.; Fang, L.; Hu, J.; Luo, H.; Guan, T.; et al. Layered NiFe-LDH/MXene nanocomposite electrode for high-performance supercapacitor. *International Journal of Hydrogen Energy* **2020**, *45*(23), 13080–13089. doi:10.1016/j.ijhydene.2020.03.001.

69. Tian, M.; Liu, C.; Neale, Z. G.; Zheng, J.; Long, D.; Cao, G. Chemically Bonding NiFe-LDH Nanosheets on rGO for Superior Lithium-Ion Capacitors. *ACS Applied Materials and Interfaces* **2019**, *11*(39), 35977–35986. doi:10.1021/acsami.9b10719.

70. Zhou, G.; Ding, W.; Guan, Y.; Wang, T.; Liu, C.; Zhang, L.; et al. Progress of NiO-Based Anodes for High-Performance Li-Ion Batteries. *Chemical Record*. John Wiley and Sons Inc October 1, 2022. doi:10.1002/tcr.202200111.

71. Yang, C. C.; Zhang, D. M.; Du, L.; Jiang, Q. Hollow Ni-NiO nanoparticles embedded in porous carbon nanosheets as a hybrid anode for sodium-ion batteries with an ultra-long cycle life. *Journal of Materials Chemistry A* **2018**, *6*(26), 12663–12671. doi:10.1039/c8ta03692f.

72. Ata-ur-Rehman; Iftikhar, M.; Latif, S.; Jevtovic, V.; Ashraf, I. M.; El-Zahhar, A. A.; et al. Current advances and prospects in NiO-based lithium-ion battery anodes. *Sustainable Energy Technologies and Assessments* **2022**, *53*, 102376. doi:10.1016/J.SETA.2022.102376.

73. Cavani, F.; Trifirò, F.; Vaccari, A. Hydrotalcite-type anionic clays: Preparation, properties and applications. *Catalysis Today* **1991**, *11*(2), 173–301. doi:10.1016/0920-5861(91)80068-K.

74. Conterosito, E.; Croce, G.; Palin, L.; Pagano, C.; Perioli, L.; Viterbo, D.; et al. Structural characterization and thermal and chemical stability of bioactive molecule-hydrotalcite (LDH) nanocomposites. *Physical Chemistry Chemical Physics* **2013**, *15*(32), 13418–13433. doi:10.1039/c3cp51235e.

75. Li, X.; Wan, G.; Xiao, J.; Wu, L.; Shi, S.; Wang, G. Carbon-coated Ni(OH)2-NiAl LDH hierarchical nanostructures on Ni foam as a high areal capacitance electrode for supercapacitor application. *Materials Letters* **2018**, *228*, 179–182. doi:10.1016/J.MATLET.2018.06.012.

76. Ardizzone, S.; Fregonara, G.; Trasatti, S. “Inner” and “outer” active surface of RuO2 electrodes. *Electrochimica Acta* **1990**, *35*(1), 263–267. doi:10.1016/0013-4686(90)85068-X.

77. Li, J.; Hwang, S.; Guo, F.; Li, S.; Chen, Z.; Kou, R.; et al. Phase evolution of conversion-type electrode for lithium ion batteries. *Nature Communications* **2019**, *10*(1). doi:10.1038/s41467-019-09931-2.

78. Pramanik, A.; Maiti, S.; Mahanty, S. Metal hydroxides as a conversion electrode for lithium-ion batteries: A case study with a Cu(OH)2 nanoflower array. *Journal of Materials Chemistry A* **2014**, *2*(43), 18515–18522. doi:10.1039/c4ta03379e.

79. Li, D.; Zhou, J.; Chen, X.; Song, H. Amorphous Fe2O3/Graphene Composite Nanosheets with Enhanced Electrochemical Performance for Sodium-Ion Battery. *ACS Applied Materials and Interfaces* **2016**, *8*(45), 30899–30907. doi:10.1021/acsami.6b09444.

80. Abellán, G.; Carrasco, J. A.; Coronado, E. Room temperature magnetism in layered double hydroxides due to magnetic nanoparticles. *Inorganic Chemistry* **2013**, *52*(14), 7828–7830. doi:10.1021/ic400883k.

81. Zysler, R.; Fiorani, D.; Dormann, J. L.; Testa, A. M. Magnetic properties of ultrafine α-Fe2O3 antiferromagnetic particles. *Journal of Magnetism and Magnetic Materials* **1994**, *133*(1–3), 71–73. doi:10.1016/0304-8853(94)90492-8.

82. Marmeggi, J. C.; Baruchel, J. Antiferromagnetic domains in nickel oxide by magnetic neutron laue diffraction. *Journal of Magnetism and Magnetic Materials* **1979**, *10*(1), 14–24. doi:10.1016/0304-8853(79)90309-3.

83. Görlin, M.; Ferreira de Araújo, J.; Schmies, H.; Bernsmeier, D.; Dresp, S.; Gliech, M.; et al. Tracking Catalyst Redox States and Reaction Dynamics in Ni–Fe Oxyhydroxide Oxygen Evolution Reaction Electrocatalysts: The Role of Catalyst Support and Electrolyte pH. *Journal of the American Chemical Society* **2017**, *139*(5), 2070–2082. doi:10.1021/jacs.6b12250.

84. Verdianto, A.; Lim, H.; Kang, J. G.; Kim, S.-O. Scalable, colloidal synthesis of SnSb nanoalloy-decorated mesoporous 3D NiO microspheres as a sodium-ion battery anode. *International Journal of Energy Research* **2022**, *46*(4), 4267–4278. doi:https://doi.org/10.1002/er.7424.

85. Zhang, Y.; Lim, Y. Von; Huang, S.; Pam, M. E.; Wang, Y.; Ang, L. K.; et al. Tailoring NiO Nanostructured Arrays by Sulfate Anions for Sodium-Ion Batteries. *Small* **2018**, *14*(28), 1800898. doi:https://doi.org/10.1002/smll.201800898.

86. Vaiopoulou, E.; Gikas, P. Regulations for chromium emissions to the aquatic environment in Europe and elsewhere. *Chemosphere*. Elsevier Ltd September 1, 2020, p 126876. doi:10.1016/j.chemosphere.2020.126876.

87. Ugulu, I.; Zafar, ·; Khan, I.; Hareem Safdar, ·; Ahmad, · Kafeel; Bashir, H. Chromium Bioaccumulation by Plants and Grazing Livestock as Affected by the Application of Sewage Irrigation Water: Implications to the Food Chain and Health Risk. *International Journal of Environmental Research* **2021**, No. 3. doi:10.1007/s41742-021-00311-7.

88. Karimi-Maleh, H.; Orooji, Y.; Ayati, A.; Qanbari, S.; Tanhaei, B.; Karimi, F.; et al. Recent advances in removal techniques of Cr(VI) toxic ion from aqueous solution: A comprehensive review. *Journal of Molecular Liquids* **2020**, 115062. doi:10.1016/j.molliq.2020.115062.

89. Kang, D.; Yu, X.; Tong, S.; Ge, M.; Zuo, J.; Cao, C.; et al. Performance and mechanism of Mg/Fe layered double hydroxides for fluoride and arsenate removal from aqueous solution. *Chemical Engineering Journal* **2013**, *228*, 731–740. doi:10.1016/j.cej.2013.05.041.

90. Kanezaki, E. Thermal behavior of the hydrotalcite-like layered structure of Mg and Al-layered double hydroxides with interlayer carbonate by means of in situ powder HTXRD and DTA/TG. *Solid State Ionics* **1998**, *106*(3–4), 279–284. doi:10.1016/S0167-2738(97)00494-3.

91. Forano, C.; Costantino, U.; Prévot, V.; Gueho, C. T. Chapter 14.1 - Layered Double Hydroxides (LDH). In *Developments in Clay Science*. Bergaya, F., Lagaly, G., Eds.; Elsevier, 2013; Vol. 5, pp 745–782. doi:https://doi.org/10.1016/B978-0-08-098258-8.00025-0.

92. Sławiński, W. A.; Sjåstad, A. O.; Fjellvåg, H. Stacking Faults and Polytypes for Layered Double Hydroxides: What Can We Learn from Simulated and Experimental X-ray Powder Diffraction Data? *Inorganic Chemistry* **2016**, *55*(24), 12881–12889. doi:10.1021/acs.inorgchem.6b02247.

93. Putman, K. J.; Rowles, M. R.; Marks, N. A.; Suarez-Martinez, I. The role of the 2D-to-3D transition in x-ray diffraction analysis of crystallite size. *Journal of Physics: Condensed Matter* **2021**, *33*(29), 294002. doi:10.1088/1361-648X/ac0083.

94. Hidber, P. C.; Graule, T. J.; Gauckler, L. J. Citric Acid—A Dispersant for Aqueous Alumina Suspensions. *Journal of the American Ceramic Society* **1996**, *79*(7), 1857–1867. doi:https://doi.org/10.1111/j.1151-2916.1996.tb08006.x.

95. Frost, M. S.; Dempsey, M. J.; Whitehead, D. E. Highly sensitive SERS detection of Pb2+ ions in aqueous media using citrate functionalised gold nanoparticles. *Sensors and Actuators B: Chemical* **2015**, *221*, 1003–1008. doi:10.1016/J.SNB.2015.07.001.

96. Zhang, L. H.; Li, F.; Evans, D. G.; Duan, X. Evolution of structure and performance of Cu-based layered double hydroxides. *Journal of Materials Science* **2010**, *45*(14), 3741–3751. doi:10.1007/s10853-010-4423-6.

97. Thommes, M.; Kaneko, K.; Neimark, A. V; Olivier, J. P.; Rodriguez-Reinoso, F.; Rouquerol, J.; et al. Physisorption of gases, with special reference to the evaluation of surface area and pore size distribution (IUPAC Technical Report). **2015**, *87*(9–10), 1051–1069. doi:doi:10.1515/pac-2014-1117.

98. Ribeiro, N. F. P.; Neto, R. C. R.; Moya, S. F.; Souza, M. M. V. M.; Schmal, M. Synthesis of NiAl2O4 with high surface area as precursor of Ni nanoparticles for hydrogen production. *International Journal of Hydrogen Energy* **2010**, *35*(21), 11725–11732. doi:10.1016/J.IJHYDENE.2010.08.024.

99. Peymani, M.; Alavi, S. M.; Rezaei, M. Preparation of highly active and stable nanostructured Ni/CeO2 catalysts for syngas production by partial oxidation of methane. *International Journal of Hydrogen Energy* **2016**, *41*(15), 6316–6325. doi:10.1016/J.IJHYDENE.2016.03.033.

100. le Saché, E.; Reina, T. R. Analysis of Dry Reforming as direct route for gas phase CO2 conversion. The past, the present and future of catalytic DRM technologies. *Progress in Energy and Combustion Science* **2022**, *89*, 100970. doi:10.1016/J.PECS.2021.100970.

101. Hussien, A. G. S.; Polychronopoulou, K. A Review on the Different Aspects and Challenges of the Dry Reforming of Methane (DRM) Reaction. *Nanomaterials* **2022**, *12*(19). doi:10.3390/nano12193400.

102. Ranjekar, A. M.; Yadav, G. D. Dry reforming of methane for syngas production: A review and assessment of catalyst development and efficacy. *Journal of the Indian Chemical Society* **2021**, *98*(1), 100002. doi:10.1016/J.JICS.2021.100002.

6. Published papers

1. Li, X.; Fortunato, M.; Cardinale, A. M.; Sarapulova, A.; Njel, C.; Dsoke, S. Electrochemical study on nickel aluminum layered double hydroxides as high-performance electrode material for lithium-ion batteries based on sodium alginate binder. Journal of Solid State Electrochemistry 2021. doi:10.1007/s10008-021-05011-y.

2. Cardinale, A. M.; Carbone, C.; Fortunato, M.; Fabiano, B.; Reverberi, A. Pietro. ZnAl-SO4 Layered Double Hydroxide and Allophane for Cr(VI), Cu(II) and Fe(III) Adsorption in Wastewater: Structure Comparison and Synergistic Effects. Materials 2022, 15(19). doi:10.3390/ma15196887.

3. Cardinale, A. M.; Fortunato, M.; Locardi, Federico; Parodi, N. Thermal analysis of MgFe-Cl Layered doubled hydroxide (LDH) directly synthetized and produced "via memory effect." Journal of Thermal Analysis and Calorimetry 2022, 147, 5297–5302. doi:10.1007/s10973-022-11207-9.

4. Cardinale, A. M.; Vecchio Ciprioti, S.; Fortunato, M.; Catauro, M. Thermal behaviour and antibacterial studies of a carbonate Mg–Al-based layered double hydroxide (LDH) for in vivo uses. Journal of Thermal Analysis and Calorimetry 2022, 148(4), 1523–1532. doi:10.1007/s10973-022-11334-3.

5. Dal Poggetto, G.; Fortunato, M.; Cardinale, A. M.; Leonelli, C. Thermal, chemical and mechanical characterization of recycled corundum powder in metakaolin-based geopolymer binder. Applied Clay Science 2023, 237, 106875. doi:https://doi.org/10.1016/j.clay.2023.106875.

6. Cardinale, A. M.; Alberti, S.; Reverberi, A. Pietro; Catauro, M.; Ghibaudo, N.; Fortunato, M. Antibacterial and Photocatalytic Activities of LDH-Based Sorbents of Different Compositions. Microorganisms 2023, 11(4), 1045. doi:10.3390/microorganisms11041045

7. Fortunato, M.; Reverberi, A. Pietro; Fabiano, B.; Cardinale, A. M. Thermal Evolution of NiFe-NO3 LDH and Its Application in Energy Storage Systems. Energies 2024, 17(5). doi:10.3390/en17051035.